









The Redshift of GRB 190829A/SN 2019oyw: A Case Study of GRB-SN Evolution.

KORNOB BHIROMBHAKDI ¹, ANDREW S. FRUCHTER ¹, ANDREW J. LEVAN,^{2,3} ELENA PIAN ⁴, PAOLO MAZZALI,^{5,6}
LUCA IZZO ^{7,8}, TUOMAS KANGAS ^{9,10}, STEFANO BENETTI ¹¹, KYLE MEDLER ⁵, AND NIAL TANVIR ¹²

¹*Space Telescope Science Institute, 3700 San Martin Dr, Baltimore, MD 21218, USA*

²*Department of Astrophysics/IMAPP, Radboud University Nijmegen, P.O. Box 9010, 6500 GL Nijmegen, The Netherlands*

³*Department of Physics, University of Warwick, Coventry, CV4 7AL, UK*

⁴*INAF, Astrophysics and Space Science Observatory, Via P. Gobetti 101, 40129 Bologna, Italy*

⁵*Astrophysics Research Institute, Liverpool John Moores University, 146 Brownlow Hill, Liverpool L3 5RF, UK*

⁶*Max-Planck Institut für Astrophysik, Karl-Schwarzschild-Str. 1, D-85748 Garching, Germany*

⁷*DARK, Niels Bohr Institute, University of Copenhagen, Copenhagen N, Denmark*

⁸*INAF - Osservatorio Astronomico di Capodimonte, Naples, Italy*

⁹*Finnish Centre for Astronomy with ESO (FINCA), FI-20014 University of Turku, Finland*

¹⁰*Department of Physics and Astronomy, University of Turku, Vesilinnantie 5, FI-20500, Finland*

¹¹*INAF - Osservatorio Astronomico di Padova, vicolo dell'Osservatorio 5, Padova I-35122, Italy*

¹²*School of Physics and Astronomy, University of Leicester, University Road, Leicester LE1 7RJ, UK*

ABSTRACT

The nearby long gamma-ray burst (GRB) 190829A was observed using the *HST*/WFC3/IR grisms about four weeks to 500 days after the burst. We find the spectral features of its associated supernova, SN 2019oyw, are redshifted by several thousands km/s compared to the redshift of the large spiral galaxy on which it is superposed. This velocity offset is seen in several features but most clearly in Ca II NIR triplet $\lambda\lambda$ 8498, 8542, 8662 Å (CaIR3). We also analyze VLT/FORS and X-shooter spectra of the SN and find strong evolution with time of its P-Cygni features of CaIR3 from the blue to the red. However, comparison with a large sample of Type Ic-BL and Ic SNe shows no other object with the CaIR3 line as red as that of SN 2019oyw were it at the $z = 0.0785$ redshift of the disk galaxy. This implies that SN 2019oyw is either a highly unusual SN or is moving rapidly with respect to its apparent host. Indeed, using CaIR3 we find the redshift of SN 2019oyw is $0.0944 \leq z \leq 0.1156$. The GRB-SN is superposed on a particularly dusty region of the massive spiral galaxy; therefore, while we see no sign of a small host galaxy behind the spiral, it could be obscured. Our work provides a surprising result on the origins of GRB 190829A, as well as insights into the time evolution of GRB-SNe spectra and a method for directly determining the redshift of a GRB-SN using the evolution of strong spectral features such as CaIR3.

Keywords: Core-collapse supernovae(304) — Gamma-ray bursts(629) — Spectroscopy(1558)

1. INTRODUCTION

The long-duration gamma-ray burst (GRB) 190829A (de Ugarte Postigo et al. 2019; Lipunov et al. 2019; Volnova et al. 2019) was detected by the *Fermi*/Gamma-ray Burst Monitor (GBM) on 29th August 2019, 19:55:53.13 UTC (henceforth, we adopted this as T_0 for the event; Fermi GBM Team (2019)), and shortly after by the *Swift*/Burst Alert Telescope (Dichiara et al. 2019). Its afterglow was detected in multiple wavelengths from X-ray to radio (Chand et al. 2020; Dichiara et al. 2022; Fraija et al. 2021; Hu et al. 2021; Salafia et al. 2022), and revealed its location to be superposed on the galaxy SDSS J025810.28-085719.2 (henceforth, we referred to this galaxy in short as the “SDSS galaxy”; for further information see skyserver.sdss.org; Abdurro’uf et al. (2022); also Figure 1).¹ Very high energy

Corresponding author: Kornpob Bhirombhakdi
bkornpob@gmail.com

¹ This SDSS galaxy is also known as 2MASX J02581029-0857189 (Skrutskie et al. 2006).

(VHE) photons in the tera-electronvolt range were detected from the event (de Naurois 2019; H. E. S. S. Collaboration et al. 2021), while the search for associated neutrinos yielded only an upper limit (ANTARES Collaboration et al. 2021). The detection of Ca II H/K $\lambda\lambda$ 3934, 3969 Å absorption in the afterglow (Hu et al. 2021; Valeev et al. 2019) gave the redshift estimate $z = 0.0785$, which is consistent with the observed redshift of that galaxy. This bright spiral has a stellar mass of order of $10^{12} M_{\odot}$ (Gupta et al. 2022), the largest stellar mass of any proposed GRB host. The galaxy also exhibits characteristics of an active galactic nucleus (AGN; Izzo et al. (in prep.); Patricia Schady via personal communication), which would be the first for a long GRB host. Moreover, the sight-line to the GRB was estimated to have $A_V = 2.33$ mag (Zhang et al. 2021), making it unusually dusty for a long GRB environment at a redshift $z < 1$. Despite being atypical for a long GRB host (Fruchter et al. 2006; Japelj et al. 2018; Kelly et al. 2014; Modjaz et al. 2020; Perley et al. 2016), the SDSS galaxy seems to be the obvious choice considering the location of the burst and the fact that all observed absorption features in the GRB spectrum appear to come from this galaxy.

Perhaps in part because it was so nearby, GRB 190829A itself was found to have a number of somewhat unusual properties. For example, the Amati correlation, which typically characterizes long GRBs (Amati 2006), was violated by one, but not another of two main emission events from this burst (Chand et al. 2020). Although it was a VHE burst displaying photons with energy above 100 GeV, its peak photon energy was among the lowest of known VHE-GRBs (see Sato et al. (2023) and references therein). It also had the smallest isotropic energy when compared to other VHE-GRBs (Abdalla et al. 2019; Blanch et al. 2020; Duan & Wang 2019; MAGIC Collaboration et al. 2019; Ravasio et al. 2019).

However, it is the supernova associated with the GRB 190829A, SN 2019oyw, which most interests us in this paper. SN 2019oyw emerged a few days after the GRB trigger (de Ugarte Postigo et al. 2019; Lipunov et al. 2019; Volnova et al. 2019), and reached its i -band peak by ~ 20 days (Hu et al. 2021). Its early spectra showed characteristic features of a type Ic-BL (Fraija et al. 2021; Hu et al. 2021), similar to other GRB-SNe (Cano et al. 2014; Modjaz et al. 2016) and in particular the prototype GRB-SN 1998bw (Patat et al. 2001). Broad absorption features of Si II λ 6355 Å and the Ca II near-infrared (NIR) triplet $\lambda\lambda$ 8498, 8542, 8662 Å (henceforth CaIR3, using the terminology of Silverman et al. (2015)) were identified (Hu et al. 2021).

In this paper (Section 2), we present late-time observations of SN 2019oyw from *HST*/WFC3 observed between 2019-09-28 and 2021-01-09 (i.e., 30 – 499 days after the trigger in the observing frame). Optical and NIR images and NIR grism data were obtained. Our analysis of these data (Section 3) shows that the spectral features associated with the supernova at late time (~ 50 days) are redshifted by several thousands of km/s compared to the redshift of the large spiral on which it is superposed. With additional data from the Very Large Telescope (VLT) provided by (Medler 2023) and Izzo et al. (in prep.), we analyze spectral features of the supernova together with a sample of GRB-SNe, SNe Ic-BL (without associated GRB), and SNe Ic, and show that SN 2019oyw is the only outlier (Section 4). We re-estimate the redshift that improves the feature alignment, and interpret this as surprising evidence that the SN progenitor exploded in or near the SDSS galaxy with a great peculiar velocity, or it was hosted by another galaxy of the order 100 Mpc behind the SDSS galaxy (Section 5). However, we find no evidence of another more distant host in the spectra or images, while the non-detection still does not rule out the possibility. Lastly, we summarize our results in Section 6.²

2. OBSERVATIONS

GRB 190829A/SN 2019oyw was observed at several epochs between 2019-09-28 and 2021-01-09 (i.e., 30 – 499 days after the trigger in the observing frame) by the Wide Field Camera 3 of the *Hubble Space Telescope* (*HST*/WFC3; Dressel (2021)). Both images and spectra were obtained in optical and NIR, as summarized in Table 1. In this section, we briefly describe the data and the reduction process for photometry and spectroscopy from the *HST*, in Subsections 2.1 and 2.2 respectively. In addition to the *HST* data, we were provided additional data from the Very Large Telescope (VLT) by Medler (2023) and Izzo et al. (in prep.). We briefly describe the VLT observations in Subsection 2.3.

2.1. *HST*/WFC3 Photometry

² We assume a Λ CDM cosmology with $H_0 = 70$ km/s/Mpc, $\Omega_m = 0.3$, $\Omega_{\Lambda} = 0.7$.

Table 1. Summary of datasets from *HST*/WFC3

Proposal ID	PI	Epoch	Channel	Filter	Total Exposure (s)		
(1)	(2)	(3)	(4)	(5)	(6)		
15089	E. Troja	2019-09-28	IR	F110W*	148		
				F160W*	148		
				G102	2012		
				G141	2012		
		2019-10-26	IR	F110W*	148		
				F160W*	148		
				G102	2012		
				G141	2012		
15510	N. Tanvir	2019-11-25	UVIS	F606W	870		
				F814W	870		
				2019-11-29	IR	F105W*	349
						F125W*	349
		F140W*	698				
		G102	4095				
		G141	4095				
		2020-01-12	UVIS			F606W	900
				F814W	900		
				IR	F105W*	349	
					F125W*	349	
					F140W*	349	
					G102	4095	
		16042	A. Levan	2020-02-11	IR	F125W*	698
F140W	1198						
G102	4095						
G141	4095						
2020-02-16	UVIS			F606W	1044		
				2020-06-24	UVIS	F606W	1044
IR	F140W					1198	
	2020-08-21				UVIS	F606W	1044
IR						F140W	1198
	16320			A. Levan	2021-01-09	UVIS	F606W
IR							F125W*
					F140W*	1746	
					G102	4095	
					G141	4095	

NOTE—a) * indicates that images taken with grism observations were included. See Dressel (2021) for details. b) All of the data presented in this table were obtained from the MAST at the Space Telescope Science Institute. The specific observations analyzed can be accessed via [doi:10.17909/yz9m-xb66](https://doi.org/10.17909/yz9m-xb66).

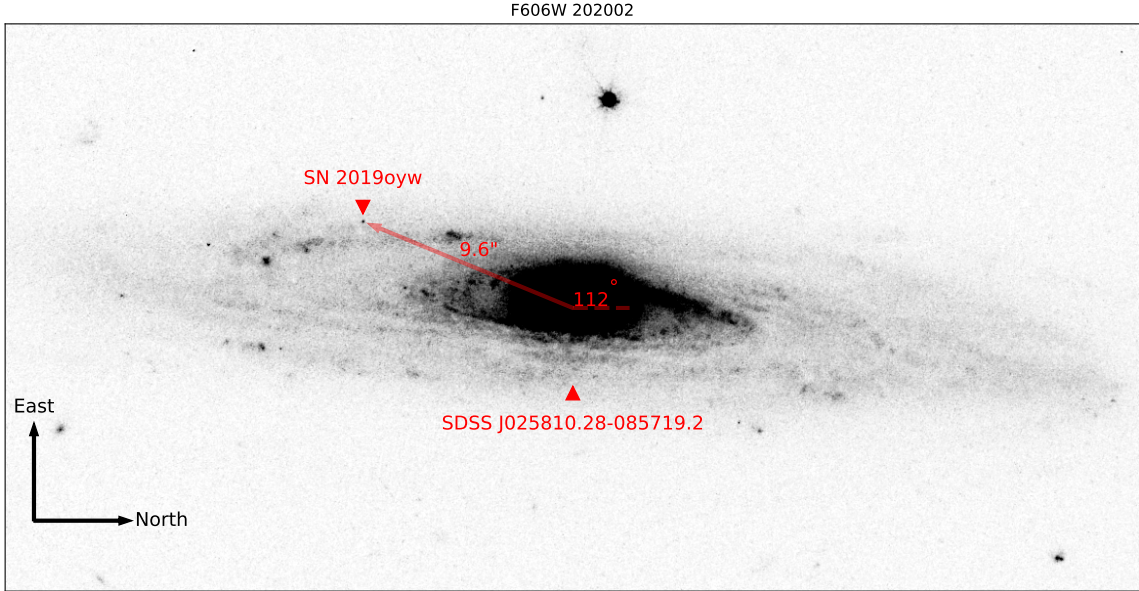


Figure 1. Image of SN 2019oyw superposing on the outer disc of SDSS J025810.28-085719.2. This image was taken with *HST*/WFC3/UVIS/F606W on 2020-02-16. SN 2019oyw was $\sim 10''$ from the brightest pixel at the galactic center in the direction $\sim 112^\circ$ with respect to north towards southeast.

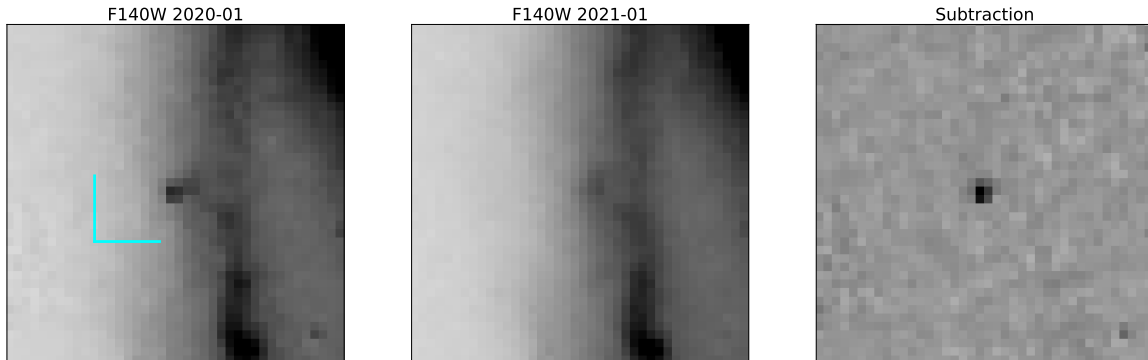


Figure 2. Images of SN 2019oyw from F140W filter. The source image taken on 2020-01-12 (LEFT) was subtracted by the template image taken on 2021-01-09 (MIDDLE), resulting in the subtracted image (RIGHT) that clearly shows the transient. These images are shown in inverted-color (i.e., black = bright). Orientation is north-up and east-left. The cyan lines show the length scale of 1 arcsecond in each direction.

Images of SN 2019oyw were taken by *HST*/WFC3 (Dressel 2021) in optical (UVIS channel) and NIR (IR channel). Table 1 summarizes the data. We followed the reduction process recommended by Sahu & et al. (2021). The data were pre-processed and downloaded from the Barbara A. Mikulski Archive for Space Telescopes (MAST; <https://archive.stsci.edu/>) in FLT/FLC format. The dithered images were combined using Drizzle (Fruchter & Hook 2002) as implemented in ASTRODRIZZLE (Gonzaga).³ Figure 1 shows an example of the processed image from F606W on 2020-02-16. The image clearly shows SN 2019oyw superposed on the outer disc of the SDSS J025810.28-085719.2 (Dichiara et al. 2019; Hu et al. 2021; Oates et al. 2019).

To perform the photometric measurement, we removed the galaxy light by template subtraction for filters F606W, F125W, and F140W where we used the observations on 2021-01-09 (499 days) as templates. We show in Figure 2 an example of the original source image (LEFT), template image (MIDDLE), and the result from the subtraction (RIGHT). The alignment was done by using nearby stars in a subset of the field-of-view. The stellar alignments were

³ <https://www.stsci.edu/scientific-community/software/drizzlepac.html>

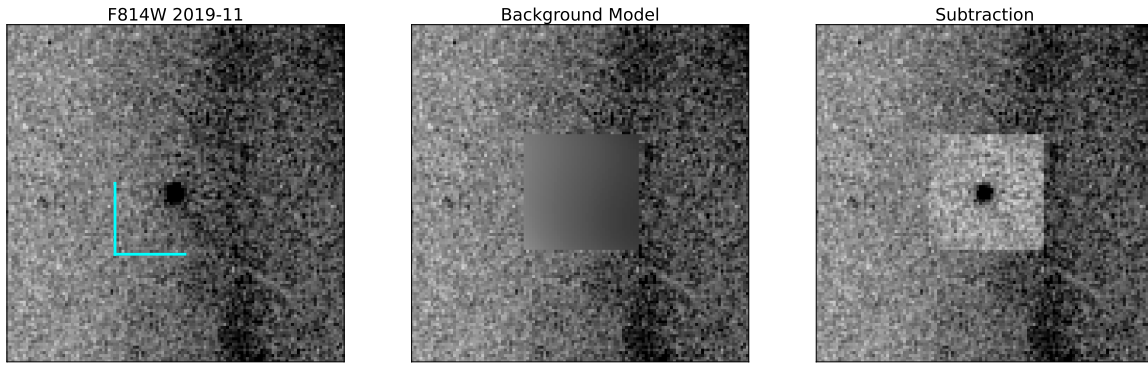


Figure 3. An image of SN 2019oyw taken by *HST*/WFC3/UVIS/F814W on 2019-11-25 (LEFT). Its background model is shown in the MIDDLE image, resulting in the subtraction image on the RIGHT. These images are shown in inverted-color (i.e., black = bright). Orientation is north-up and east-left. The cyan lines show the length scale of 1 arcsecond in each direction.

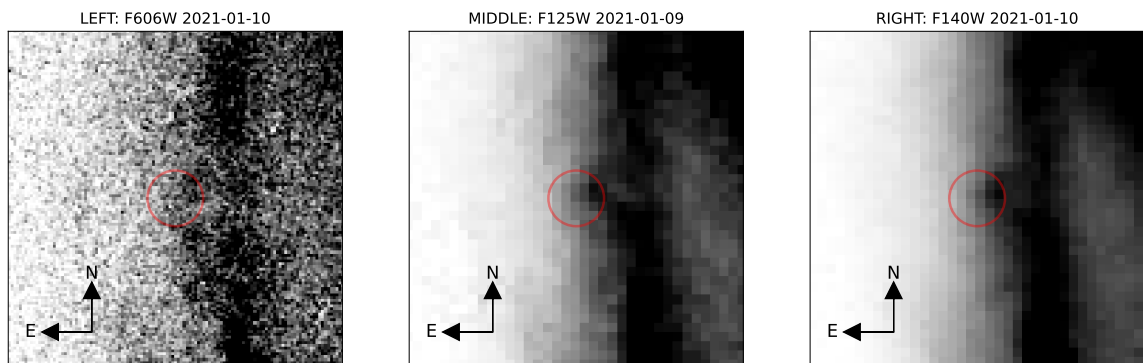


Figure 4. Environment of GRB 190829A/SN 2019oyw in F606W, F125W, and F140W. Images were taken in January 2021, and are shown in inverse color, i.e., black = bright. The event was located at the center. Each red circular aperture is the size of 0.39 arcsecond in radius (i.e., 3 pixels in WFC3/IR and 9.75 pixels in WFC3/UVIS images). We observed a dust lane extending from north to south westwards from the aperture. We noted a bright clump (noticeable especially in F125W and F140W) associated with the dust lane on the western edge of the aperture.

accurate to the order of 0.1 pixel. We note some complications met when reducing some of these data. For F140W, 2020-02-11, we only combined the observations dedicated for imaging, and excluded the direct images associated with G141 grism observation. This is because the direct images associated with the grism were taken using a different part of the chip, and the distortion solutions are sufficiently inexact that the overall subtraction is better without these data, even though the total integration is somewhat shorter by excluding them (i.e., 1,200 vs. 1,900 seconds). For F140W, 2020-06-24, there was scattered light from out of the field causing the estimated upper limit to be brighter than it would have been in an uncontaminated part of the field.

For the other filters where we did not observe a template, we modelled the image around the source with two components: a point source as a 2D gaussian for the transient component, and the galaxy component as a smooth background modelled by a low-order polynomial. We implemented this using the *ASTROPY* package (Astropy Collaboration et al. 2013, 2018). Figure 3 shows an example of the described procedure. From the source image (LEFT), the two-component model was fitted to the data given a region centered on the transient. We used the background component (MIDDLE) for the subtraction (RIGHT).

We note that in the template images (Figure 4) a clump, located slightly to the north and west of the SN, is noticeable in F125W and F140W, but less noticeable in F606W. Our background models with low-order polynomials cannot capture the clump. However, the method was only applied to observations from epochs 2019-09 to 2020-01, when the transient was visibly brighter than the background. To estimate the uncertainties, in order to compare with the template subtraction method we repeated the reduction process with images on 2020-01 in F606W, F125W, and F140W by applying background modelling method. We found that the subtracted images from the background models

Table 2. Photometry of SN 2019oyw.

Filter	2019-09	2019-10	2019-11	2020-01	2020-02	2020-06	2020-08
(1)	(2)	(3)	(4)	(5)	(6)	(7)	(8)
F606W	-	-	24.64(0.03)	25.24(0.04)	25.97(0.08)	>27.42	>27.45
F814W	-	-	23.31(0.02)	24.32(0.04)	-	-	-
F105W	-	-	22.60(0.02)	23.63(0.04)	-	-	-
F110W	20.21(0.00)	21.46(0.01)	-	-	-	-	-
F125W	-	-	22.69(0.02)	23.77(0.05)	24.64(0.09)	-	-
F140W	-	-	23.17(0.02)	24.29(0.05)	25.33(0.12)	>26.21	>26.47
F160W	20.47(0.01)	21.98(0.03)	-	-	-	-	-

NOTE—a) Unit is in AB-magnitude. b) One-sigma uncertainties are in parentheses. c) Upper limits are 3-sigma above zero. d) These values are uncorrected for extinction. e) Epochs are shorten to only YYYY-MM format for better readability. f) Note that for F606W, F125W, and F140W we used the epoch 2021-01 as a template for host subtraction, while background models were used for the other filters (see Subsection 2.1). g) Due to the lack of templates for filters F814W, F105W, F110W, and F160W, we estimate systematic uncertainties to be about 10% on epoch 2020-01, and should be proportionately less for earlier epochs. See text.

are consistently under-subtracted, when compared to the template subtraction. The difference of the photometric measurements between the two methods is about 6.5% (F606W), 13.4% (F125W), and 32.6% (F140W). Since the F814W and F105W images on 2020-01 were processed by the background modelling method, the uncertainties of these photometric measurements should be approximately 10% (if assuming a monotonic trend of the uncertainties considering the observed wavelengths). For the 2019-10 epoch of F160W, we also estimate an error of $\sim 10\%$.

Aperture photometry was performed using the PHOTUTILS package (Bradley et al. 2020).⁴ An aperture with radius of 3 pixels was used for WFC3/IR observations (i.e., ~ 0.39 arcsecond), and 4 pixels for UVIS (i.e., ~ 0.16 arcsecond). Aperture correction (from finite to infinite aperture) was done following the tables given in Dressel (2021). For a non-detection, we report a 3σ upper limit (above zero) instead. Uncertainties were propagated for the template subtraction, while we assumed negligible uncertainties from the low-order polynomial background model. Table 2 summarizes the photometry in apparent AB-magnitude. Figure 5 shows the light curve.

The data shows SN 2019oyw fading continuously until the last detection on 2020-02-16 (171 days after trigger in the observer’s frame). In the figure, we additionally show the early *i*-band light curve from (Hu et al. 2021) for comparison (in gray), which shows a consistent decline from the *i*-band peak. We note that the SDSS *i*-band is approximately comparable to the F814W of *HST*/WFC3. The decline rates from NIR bands are about 0.05 mag/day in observing frame between 2019-09 (29 days) and 2019-10 (57 days), which is slower than the optical decline rate implied by the *i*-band. Then, the decline rates turn to be slower at later times in both optical and NIR. SN 2019oyw evolved as expected for a typical GRB-SN by showing the late-time decline rates being consistent with being powered by ^{56}Co with the γ -rays not fully trapped (Nakamura et al. 2001; Woosley & Bloom 2006).

2.2. *HST*/WFC3 Spectroscopy

The spectroscopic observations of SN 2019oyw were observed by grisms G102 (8,000 – 11,500 Å) and G141 (10,750 – 17,000 Å) with the WFC3/IR channel (Dressel 2021) in six epochs (see Table 1). We reduced the data using the recommended grism reduction procedure (Sahu & et al. 2021) and the Python version of the HSTAXE package.⁵ In brief, the pre-processed data in FLT format can be downloaded from MAST (<https://archive.stsci.edu/>). With the

⁴ <https://photutils.readthedocs.io/en/stable/>

⁵ <https://www.stsci.edu/scientific-community/software/axe>

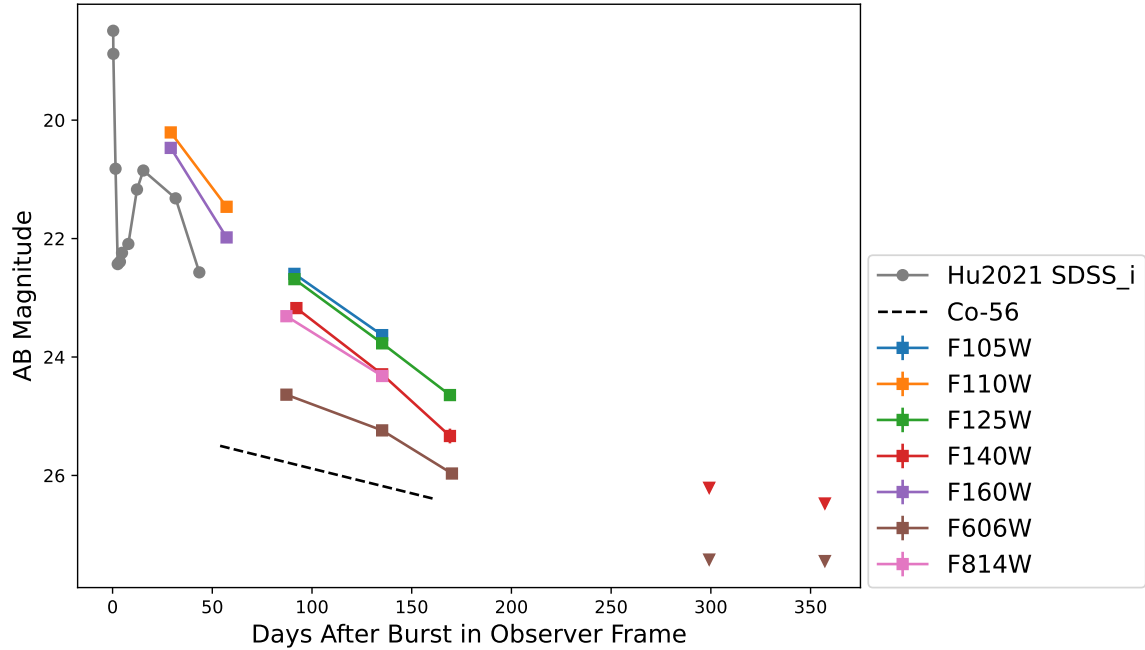


Figure 5. Light curves of SN 1919oyw. From the late-time observations, data points are squares for detections, and triangles for 3-sigma upper limits. For comparison, the plot also shows observations presented in [Hu et al. \(2021\)](#) in SDSS’s *i*-filter (gray dots), and the expected light curve’s slope if powered by fully-trapped Co^{56} (black dashed line). These values are uncorrected for Galactic and Extragalactic extinction.

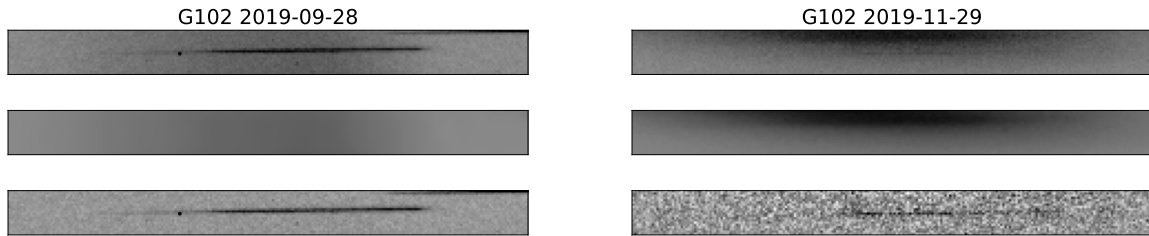


Figure 6. Grism images of SN 1919oyw and their background subtractions. LEFT: G102 image on 2019-09-28 (TOP), its background model (MIDDLE), and subtraction image (BOTTOM). RIGHT: G102 image on 2019-11-29 (TOP), its background template from epoch 2021-01-09, and subtraction image (BOTTOM). These images are shown in inverted-color (i.e., black = bright).

source’s location known from the associated direct images, the software can identify the source’s trace, and calibrate its wavelengths in the grism images. The reduction procedure continues by performing flat-field calibration, modelling and subtracting the background around the target’s trace, extracting the 1D spectrum, and calibrating the fluxes. We also used the recommended *axedrizzle* function ([Kuemmel et al. 2005](#)) for co-adding spectra from dithered observations.

The templates observed on 2021-01-09 were performed with approximately the same spacecraft orientation as the observations on 2019-11-29 and 2020-01-12 to simplify and optimize the spectral template subtraction. (We note that the source was not detected on the epoch 2020-02-06). We used DRIZZLEPAC to generate the master template by co-adding dithered images of the template, and blotted the master template back to the orientation of each source image. Then, the blotted image was subtracted from the source image. The resulting image was then used in HSTAXE for the reduction of the 1D spectrum. Figure 6 RIGHT shows an example of this procedure: the source image (TOP), the master template (MIDDLE), and the resulting image from subtraction (BOTTOM).

For observations on 2019-09-28 and 2019-10-26, we did not observe templates for subtraction. The light contamination, mainly contributed by the SDSS galaxy, was removed by modelling. To do this, since the developer’s version of the HSTAXE (which we had access to) did not have the routine for “local background” estimation available, we instead used

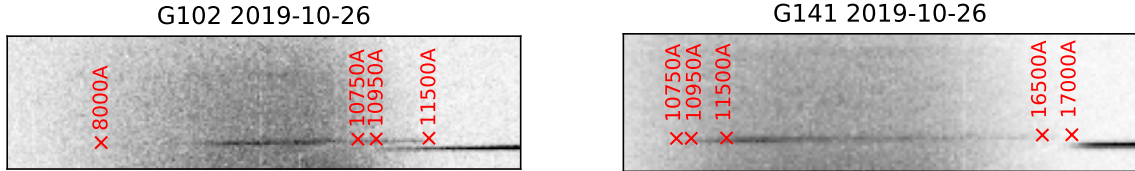


Figure 7. Grism images on 2019-10-26 epoch in G102 (LEFT) and G141 (RIGHT). Red markers mark corresponding wavelengths on SN 2019oyw’s traces. We note the markers 10,750 and 11,500 Å specifying the overlapping region between both filters. Another trace, which is visible at the bottom right of each image, was from another nearby star. The vertical separation along y-axis of the traces is 4 pixels in both filters. For G102, the star’s trace contaminates starting at 10,950 Å. For G141, SN 2019oyw’s trace is truncated at the red end due to low signal-to-noise, and for this epoch we could extract meaningful information up to about 16,500 Å, where the contamination is insignificant. We note also the truncation of the spectrum at the blue end on G102 due as well to low signal-to-noise.

the package `HSTGRISM` (<https://pypi.org/project/hstgrism/>), that can perform this task in a similar fashion. The local background estimation (see also <https://github.com/spacetelescope/hstaxe>) specifies a mask over the target’s trace. Then, given pixels above and below the trace mask at each wavelength (i.e., along X-axis) it performs 1D interpolation in the cross-dispersion direction (i.e., along Y-axis) assuming a low-order polynomial model. Then, a 2D Gaussian smoother is applied over the estimated background region to reduce the noises. Our best estimate specifies the trace mask of 7 pixels (in Y-axis, centered on the trace), polynomial order 2, and 3 pixels for the 2D Gaussian’s sigma. Figure 6 LEFT shows an example of this procedure: the source image (TOP), the background model (MIDDLE), and the resulting image from subtraction (BOTTOM).

After the galaxy-light removal, the resulting images were inputs to the `HSTAXE`. We configured the software so that the `HSTAXE` performed a simple box extraction and co-added using `axedrizzle`. We obtained the 1D spectra with uncalibrated fluxes due to the finite aperture. To calibrate to the infinite-aperture values, we adopted the aperture correction presented in [Kuntschner et al. \(2011\)](#).

We also examined contamination from other nearby sources. There is a trace of a bright star locating near the red tails of the source’s traces for both G102 and G141 on epochs 2019-09-28 and 2019-10-26. However, the contamination was insignificant. Specifically, on 2019-09-28 the stellar trace is well-separated from that of the GRB-SN (see on Figure 6 LEFT; the star’s trace is shown on the top right corner of the figure). For 2019-10-26, the contamination was also not a problem as shown in Figure 7. For G102 (Figure 7, LEFT), the contamination starts around 10,950 Å. We corrected this by using the overlapping region from the G141 observation (Figure 7, RIGHT). For G141, SN 2019oyw’s trace loses its signal strengths at long wavelengths, and we could extract meaningful information to about 16,500 Å, where the contamination was still insignificant.

Figure 8 shows the reduced late-time spectra in the observing frame. The photometric data are also shown in the figure for flux comparison, which verifies a consistent calibration between the photometry and spectroscopy. The figure shows the declining flux density and narrowing of the spectral features with time. Note that we have cropped the three later spectra at the blue and red ends, compared to the 2019-09-26 spectrum (in magenta), due to the decrease in SNR as the source fades. Two prominent features are marked on the 2019-10-26 spectrum (in blue): ‘A’ and ‘B’ at about 9,500 and 12,000 Å, respectively. These features are visible starting 2019-09-28. Feature ‘B’, although lower SNR, was also visible on 2019-11-19 (in green). The observed spectrum on 2020-01-12 (in yellow) has such low SNR that we cannot identify any feature.

2.3. VLT Spectroscopy

Additional to observations from the *HST*, [Medler \(2023\)](#) and [Izzo et al. \(in prep.\)](#) provided us with their spectroscopic observations with the VLT for the analysis in this work. From [Medler \(2023\)](#), four epochs prior to the *HST* observations were observed by the VLT/FOcal Reducer and low dispersion Spectrograph (FORS; [Appenzeller et al. \(1998\)](#)): 2019-09-02 (4 days after the trigger in observing frame), 2019-09-10 (12 days), 2019-09-15 (17 days), and 2019-09-20 (22 days). The VLT/FORS observations cover the wavelength range 3,300 – 11,000 Å. In Section 4, we combine this early VLT/FORS data with our later observations from *HST* to study the evolution with time of the Ca II NIR triplet $\lambda\lambda$ 8498, 8542, 8662 Å (see Figure 11). [Izzo et al. \(in prep.\)](#) used the VLT X-shooter ([Vernet et al. 2011](#)) to observe on 2021-09-11 and 2021-11-12. We were provided the 2D reduced spectrum (Figure 15) from the combined observations. These data reveal the spectrum of the environment at the location of the transient, which we use in our

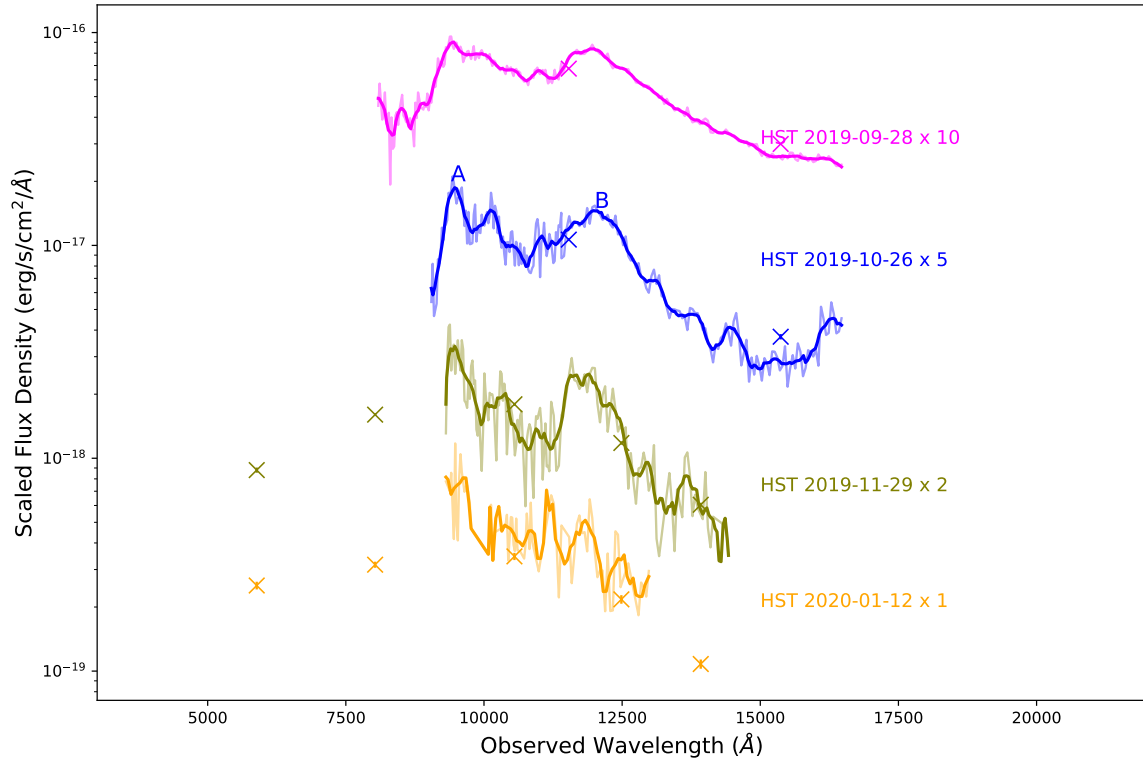


Figure 8. Spectral energy distribution of SN 2019oyw from several grism spectra taken between 2019-09-28 to 2020-01-12 using *HST*/WFC3. The plot shows raw spectra (faint lines) and their smoothed versions (solid lines).^b Each spectrum was scaled vertically for visual clarity, and the corresponding scale factor is provided. The data points shown with crosses are the photometric observations (see Table 2) shown for comparison. ‘A’ and ‘B’ mark two prominent features (at about 9,500 and 12,000 Å, respectively) observed more clearly on 2019-10-26 spectrum. The observed flux densities are shown, and are not corrected for the extinction.

^a We applied the generalized Savitzky-Golay method (Quimby et al. 2018) in smoothing the spectra. The resolution parameter was set to 60 (which is equivalent to the half width of 5,000 km/s), and the polynomial order was set to $n = 2$, excepts the spectrum on 2020-01-12 using $n = 0$ because of low SNR.

^b We applied the generalized Savitzky-Golay method (Quimby et al. 2018) in smoothing the spectra. The resolution parameter was set to 60 (which is equivalent to the half width of 5,000 km/s), and the polynomial order was set to $n = 2$, excepts the spectrum on 2020-01-12 using $n = 0$ because of low SNR.

discussion in Section 5. A full discussion of these VLT data and their implications for the GRB 190829A/SN 2019oyw will be provided in Medler et al. (in prep.) and Izzo et al. (in prep.).

3. OFFSETS OF SPECTRAL FEATURES AND REDSHIFT RE-ESTIMATION

We start our analysis by comparing the late-time *HST* spectra of SN 2019oyw with spectra of SN 1998bw (Patat et al. 2001), which has served as an archetype of GRB-SNe (Cano et al. 2014; Modjaz et al. 2016). In Figure 9 upper panel, we show SN 2019oyw’s spectrum at the epoch 2019-10-26 (the solid red line). This corresponds to a rest-frame phase of 53 days from the GRB trigger at $z = 0.0785$, the redshift of the SDSS galaxy. The letters ‘A’ and ‘B’ again mark the two prominent peaks at about 8,700 and 11,000 Å in rest-frame, respectively. The black dashed line and the black solid line show spectra of SN 1998bw on 1998-06-12, or phase 47 days, and 1998-06-24, phase, 59 days, respectively. These two spectra, obtained from WISerEP (<https://www.wiserep.org/>; Yaron & Gal-Yam (2012)), are combined here to cover a rest-frame wavelength range roughly equivalent to that observed using the G102 and G141 grisms on SN 2019oyw. Black vertical lines mark the rest wavelengths of the emission line of CaIR3 (for the Ca II NIR triplet $\lambda\lambda$ 8498, 8542, 8662 Å) and He I (for the He I λ 10830 Å).

Immediately, one notices that the features of the two transients appear offset. To better understand this issue, we experimented by assuming different redshifts for SN 2019oyw, and found an approximate redshift of $z = 0.1$. We improved upon this using cross-correlation (see Appendix A for details) arriving at a best estimate of $z^* = 0.1051$.

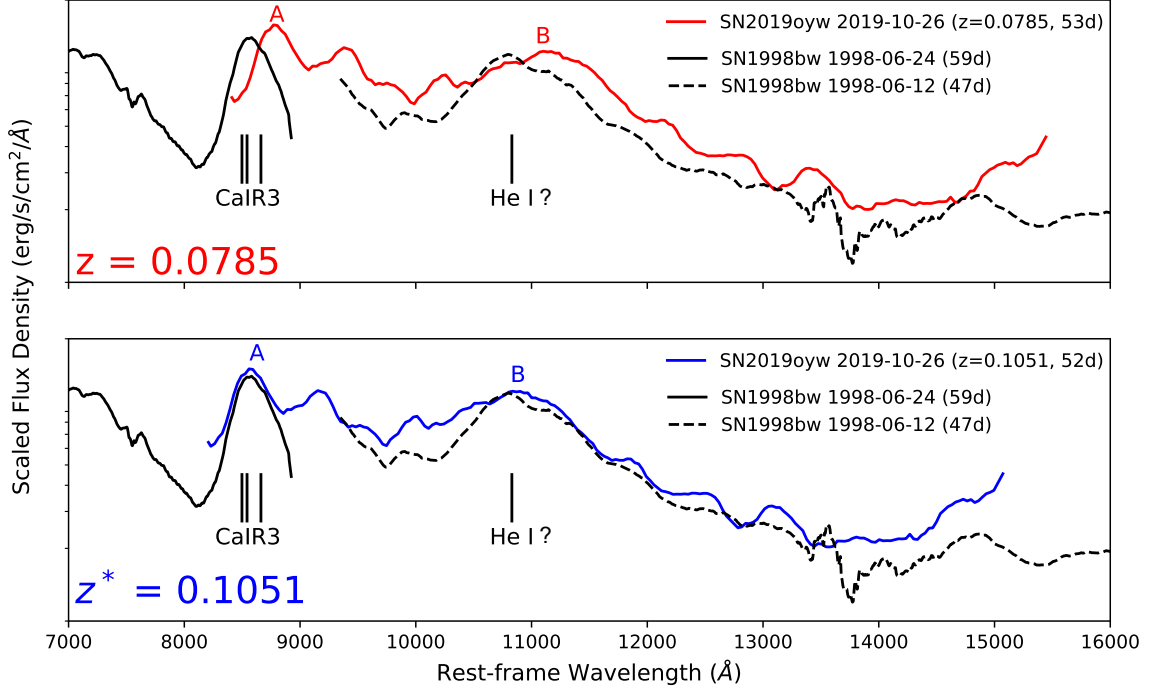


Figure 9. Alignment of SN 2019oyw’s late-time spectral features. Both panels show rest-frame wavelength on the x-axis, and on the y-axis the flux densities which are scaled for visual clarity. Upper Panel: Redshift $z = 0.0785$ is assumed for SN 2019oyw on epoch 2019-10-26 (red, phase 53 days) as the source. The letters ‘A’ and ‘B’ mark two prominent peaks in the spectrum. Spectra of both objects were extinction-corrected. SN 1998bw is chosen as the standard GRB-SN template (Cano et al. 2014; Modjaz et al. 2016). Epochs 1998-06-12 (black dashed line, 47 days) and 1998-06-24 (black solid line, 59 days) cover rest-frame wavelengths comparable to our observations in G102 and G141 grisms, and are comparable in phase to our observations of SN 2019oyw. The Ca II NIR triplet $\lambda\lambda$ 8498, 8542, 8662 Å (CaIR3) and He I λ 10830 Å are markers close to A and B, respectively. For SN 2019oyw, we adopted values $E(B - V) = 0.049, 0.757$ for Galactic (Schlafly & Finkbeiner 2011; Hu et al. 2021) and Extragalactic (Milky-Way model) reddening (Zhang et al. 2021), respectively. For SN 1998bw, we adopted $E(B - V) = 0.059$ and its host’s $A_V = 0.17$ assuming Small Magellanic Cloud dust model (see Li et al. (2018) and references therein). Lower Panel: Similar to the upper panel but assuming $z^* = 0.1051$ for SN 2019oyw instead (blue, phase 52 days). By comparing between the two cases, it is evident that assuming z^* improves the alignment.

(We will discuss the errors of this estimate later, when we further discuss the time evolution of the CaIR3 in the following section). In Figure 9 lower panel, the redshift z^* is instead assumed for SN 2019oyw (in blue solid line). Assuming z^* shows better feature alignment across the *entire* spectrum. This implies that the features ‘A’ agrees well with the wavelength of the CaIR3 complex, and feature ‘B’ with He I; however, as described in the Discussion (Section 6), there are good reasons to believe that elements other than He may be responsible for this feature.

We build upon this in Figure 10 by including the spectrum from the epoch 2019-09-28. At the redshift of $z^* = 0.1051$, this is equivalent to phase 27 days. The spectrum of SN 2019oyw (in pink solid line) is shown against SN 1998bw on 1998-05-23 (in black dotted-dashed line) which also is at phase 27 days. We repeat the epochs from ~ 50 days in this figure to better allow comparison. The plot shows consistent alignment of SN 2019oyw’s prominent feature ‘A’ in both epochs, again assuming $z^* = 0.1051$. (SN 1998bw’s spectrum at the earlier epoch does not extend sufficiently in the red to check the alignment of feature ‘B’). However, the alignment of both epochs strongly supports the contention that SN 2019oyw has an apparent redshift which is significantly greater than that of the large spiral on which it is superposed.

4. EVOLUTION OF CALCIUM II NIR TRIPLET DURING LATE PHOTOSPHERIC PHASE IN SUPERNOVAE TYPE IC-BL AND IC

We show in the previous section that by assuming $z^* = 0.1051$, instead of $z = 0.0785$, the late-time spectral features of SN 2019oyw can be much better aligned with templates from SN 1998bw. The cross correlation we used for fine-tuning the redshift works by aligning the CaIR3 peaks of the source and the template (see Appendix A). However, as

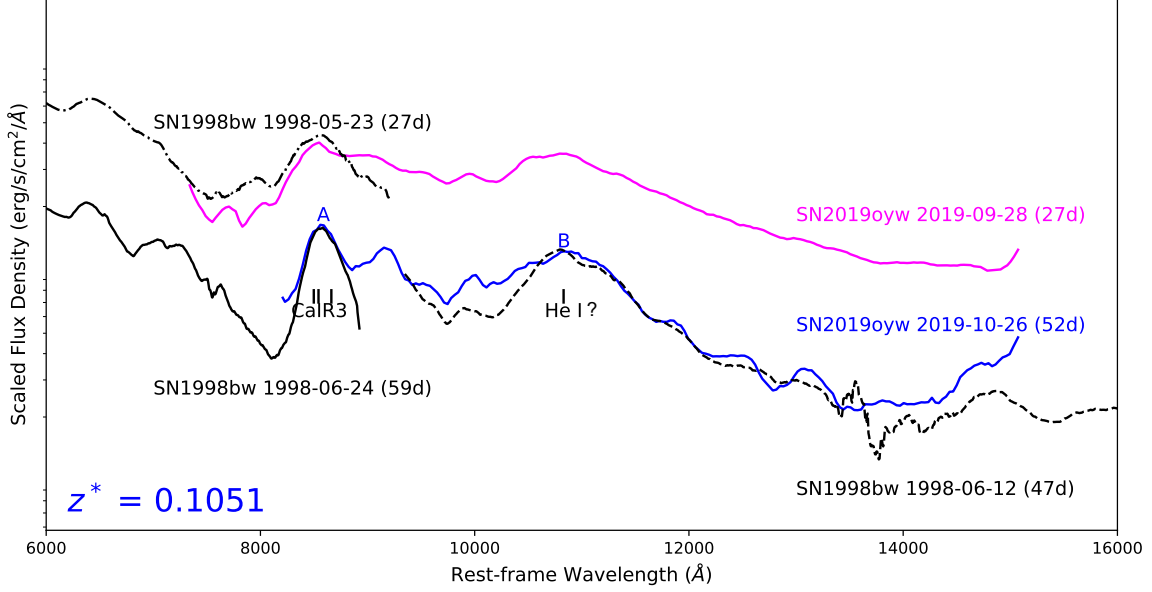


Figure 10. Alignment of SN 2019oyw’s late-time spectral features assuming $z^* = 0.1051$. The figure shows rest-frame wavelength on the x-axis, and on the y-axis the flux densities which are scaled for visual clarity. Spectra on epochs 2019-09-28 (magenta, 26 days), and 2019-10-26 (blue, 52 days) are shown (omitting epochs 2019-11-29 and 2020-01-12 spectra due to low signals). Spectra of SN 1998bw at similar phases are shown for comparisons. These spectra were extinction corrected. The figure supports consistency of the feature alignment assuming z^* .

we will discuss in this section, this feature and its peak wavelength will change over time as the expanding photosphere slows. Here, we investigate the time evolution of the CaIR3 feature and compare SN 2019oyw with samples of SNe Ic-BL and Ic.

Figure 11 shows the time evolution of CaIR3 observed on SN 2019oyw’s spectra from 2019-09-02 to 2019-10-26. Prior to three weeks after the explosion we use, with permission, VLT/FORS spectra from (Medler 2023) (see also Subsection 2.3). Later spectra are the *HST* observations presented above. The CaIR3 feature displays a characteristic P-Cygni profile. This implies the supernova is in its photospheric phase (Sim 2017) throughout. We note that for a supernova the transitioning between photospheric and nebular phases is typically about 100 days after explosion (Prentice et al. 2022). The feature and its peak are clearly seen to migrate from blue to red with time.

Figure 12 shows the time-evolution of CaIR3 features of SN 1998bw (Patat et al. 2001). The CaIR3 feature of this archetypal GRB-SN evolved in a very similar fashion. For comparison, we also plot SN 2019oyw’s CaIR3 feature from epochs 2019-09-28 (26 days) and 2019-10-26 (52 days) assuming $z^* = 0.1051$ in the figure along with the SN 1998bw data. The alignment of these two SNe supports the matching of the evolution of the P-Cygni profiles of CaIR3 if z^* is assumed.

With both GRB-SNe 1998bw and 2019oyw showing similar evolution of the CaIR3 feature during the photospheric phase, we further investigate this commonality by showing the evolution of the CaIR3 peak emission in a larger sample of Type Ic-BL SNe in Figure 13. The sample includes SNe both with and without associated GRB. (See Modjaz et al. (2016) and references therein for further references of these objects). The figure shows the rest-frame wavelength of the evolving CaIR3 peak (in each object’s rest frame) on the x-axis, and the associated phases on y-axis. SN 2019oyw’s CaIR3 peak is shown in the figure in blue (assuming $z^* = 0.1051$) and red (assuming $z = 0.0785$). In the figure, we observe similar evolution of CaIR3 peaks migrating from blue towards red with age. The figure shows that the apparent peaks at early phases can be bluer than 8,498 Å, the bluest of the CaIR3 lines. However, the evolution eventually brings the peaks back to be consistent with the CaIR3 interval during late photospheric phase. Most objects show their CaIR3 peaks residing inside the rest-frame CaIR3 wavelength range starting from 30 to 100 days. An exception is GRB-SN 2010bh which possessed significantly higher expansion velocity than the standard GRB-SN 1998bw at similar phases (Bufano et al. 2012; Chornock et al. 2010).

Similarly, Figure 14 shows the evolution of CaIR3 peaks from a sample of SNe Ic (square data points; see also Modjaz et al. (2016) and references therein). We note that, for a SN without GRB, which is the case for all these

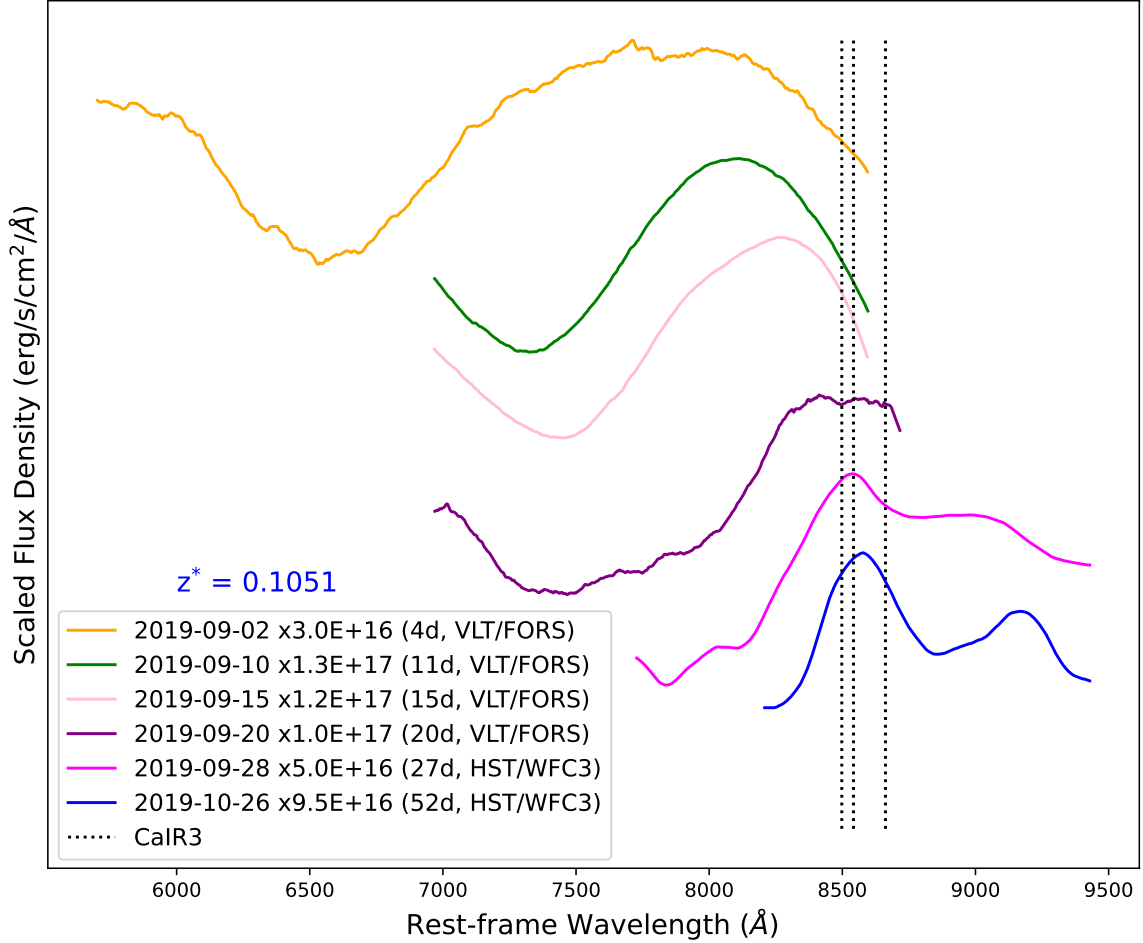


Figure 11. Evolution of SN 2019oyw’s CaIR3 feature. The spectra in this plot show the evolution of the CaIR3 feature from 4 days after burst to 52 days after burst (in rest-frame, assuming $z^* = 0.1051$). The spectra are scaled for legibility and do not represent the evolution of the spectral flux; the scaling factors are provided in the legend. The peak evolves from the blue back towards the restframe wavelengths of the CaIR3 interval as the expansion of the photosphere slows. As we will discuss, this is a common feature of Type Ic and Ic-BL supernovae, and understanding this time evolution is critical for accurately estimating the true redshift of SN 2019oyw. These spectra are extinction corrected, and smoothed (see Subsection 2.2 for details) .

SNe Ic, phase is referred from the date of discovery. The data for these transients were downloaded from WISeREP (<https://www.wiserep.org/>; Yaron & Gal-Yam (2012)), and we verified other relevant information such as the date of discovery and redshift from the Transient Name Server (<https://www.wis-tns.org/>). Like SNe Ic-BL, their CaIR3 peaks evolve to be redder with time; unlike SNe Ic-BL, most of the SNe Ic do not exhibit a CaIR3 peak bluer than the CaIR3 interval, due to their smaller expansion velocities. Shown among the sample, PTF 12gzk is an example of Type Ic that behaved more similarly to the Type Ic-BL by exhibiting a bluer peak than the interval at early photospheric phase with a rapid motion to redder wavelengths, then transition to a slow motion once the peak already resides within the interval. We note that PTF 12gzk was an unusual Type Ic exhibiting fast ejecta expansion velocities similar to Type Ic-BL but not persistent broad lines (Ben-Ami et al. 2012).

We observe from the SNe Ic sample that their CaIR3 peaks slowly become redder while residing inside the CaIR3 interval through the late photospheric phase until about 100 days, similar to the Ic-BL sample. Beyond this, moving into the nebular phase some objects show CaIR3 peaks redder than 8,662 Å, which may be explained by contributions from [C I] λ 8727 and Fe II λ 8830 (Prentice et al. 2022).

From these samples, we note three key observations:

1. For each object, the peak of the CaIR3 evolves from blue to red with time, with this evolution being particularly rapid at early epochs when the peak is observed to be bluer than the bluest line in the triplet, i.e., 8,498 Å.

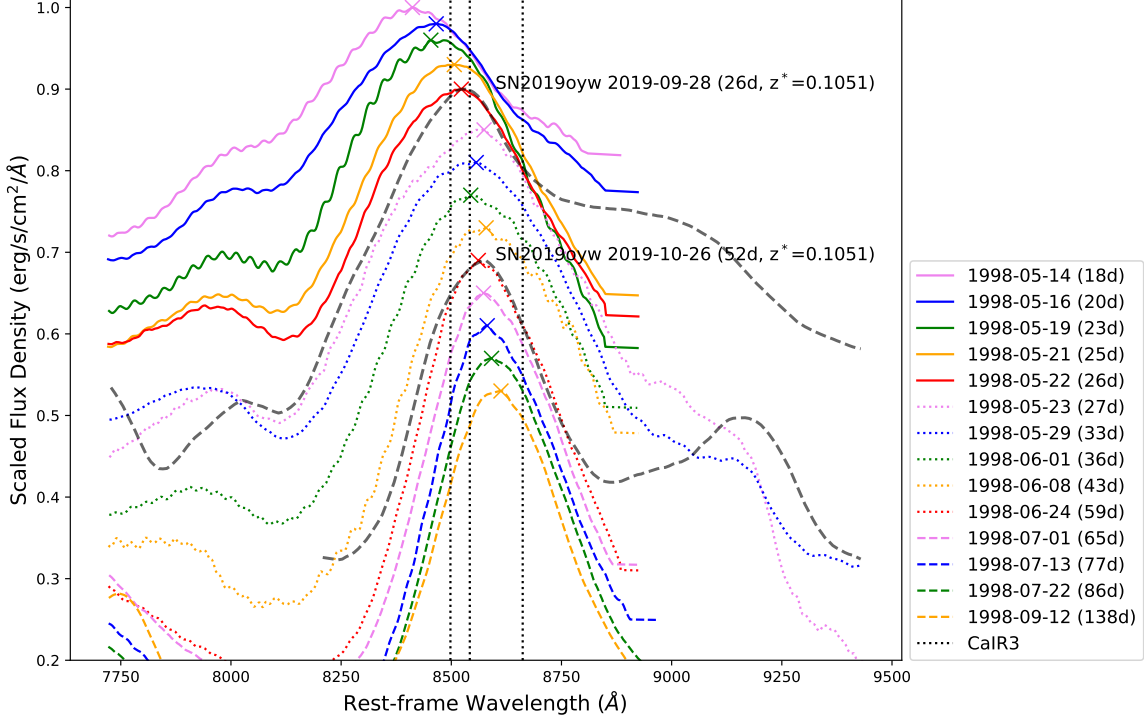


Figure 12. Evolution of SN 1998bw’s CaIR3 emission. The figure shows rest-frame wavelengths on x-axis, and flux densities on y-axis are scaled for visual clarity SN 1998bw’s spectra from 1998-05-14 (18 days) to 1998-09-12 (138 days) are shown ordering from top to bottom by epoch (Patat et al. 2001). The figure features peaks of CaIR3 (marked by crosses). The evolution shows that the peaks become redder with age. They started to be inside the constraint starting at phase 25 days, and stayed inside the constraint until at least 138 days. We discuss more about the evolution in Subsection 4. Spectra of SN 2019oyw on epochs 2019-09-28 and 2019-10-26 (black dotted lines) are also shown in the figure (assuming $z^* = 0.1051$) for comparisons with SN 1998bw at similar phases. These spectra were smoothed by the generalized Savitsky-Golay method (Quimby et al. (2018); see Subsection 2.2 for details), and extinction corrected. We also note that the small oscillation (also known as “fringing”) observed on some of SN 1998bw’s spectra (e.g., 18 and 23 days) is the feature seen in the original data, not an artifact from our process.

2. However, the CaIR3 peak evolves more slowly inside the interval, i.e., $8,498 \leq \lambda_{\text{CaIR3}} \leq 8,662 \text{ \AA}$.
3. The peaks are well constrained within the CaIR3 interval at late photospheric phase (typically after 30 days), as the curve turns nearly vertical at this phase.

In Figures 13 and 14, SN 2019oyw is displayed assuming both $z = 0.0785$ (red) and $z^* = 0.1051$ (blue). The data show the evolution of the CaIR3 peak of SN 2019oyw follows a typical path if z^* is assumed. However, if $z = 0.0785$ is assumed, the CaIR3 peak of SN 2019oyw is significantly redder than any other SN in the sample, and at late times the observed spectral peak would have to somehow be transferred to another set of line or lines redder than the CaIR3 triplet. The primary suspect for these lines would be [C I] λ 8727 and Fe II λ 8830, which tends to appear in the nebular phase (Prentice et al. 2022). Therefore, we think this explanation is unlikely.

Given the samples, the uncertainties from our cross-correlation result of z^* (see Appendix A) are dominated by two important choices we made, rather than the statistics from the cross-correlation technique itself. First, we chose the epoch 2019-10-26 for the cross-correlation as this is clearly already on the slow motion part of the CaIR3 peak’s evolution which we think began around the epoch 2019-09-28. Assuming that the epoch 2019-10-26 is on the slow motion part, to behave like the other SNe in the sample, the peak wavelength must reside inside the CaIR3 interval. However, where exactly the peak should be inside the interval depends on the choice of the template. *Therefore, a conservative method to estimate the redshift uncertainty is to ask what redshift is required to move the CaIR3 peak on 2019-10-26 inside the CaIR3 interval, i.e., $8,498 - 8,662 \text{ \AA}$. This redshift range is $0.0944 \leq z^* \leq 0.1156$, and we use this interval as our final estimate of z^* .* We note that this estimate is derived from the samples of SNe Ic-BL and Ic presented above, not only from the SN 1998bw.

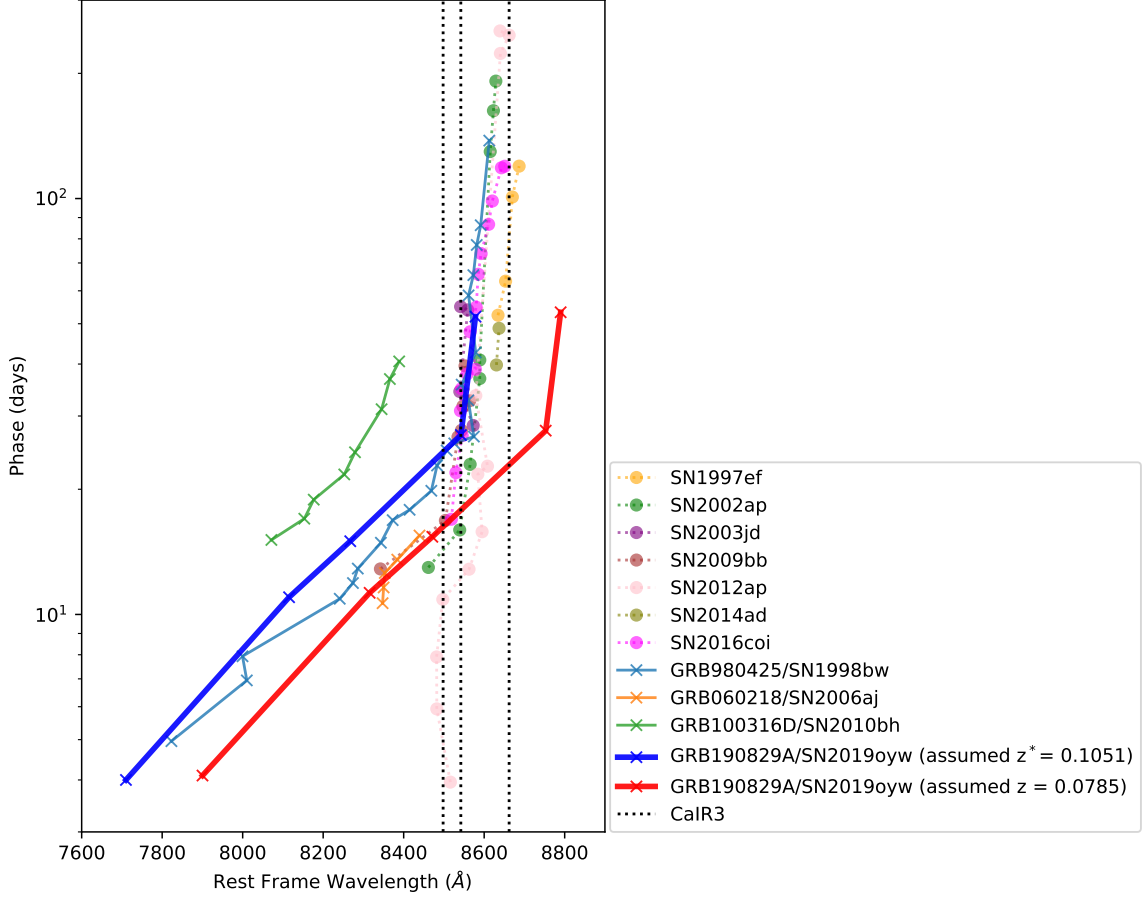


Figure 13. Evolution of CaIR3 peaks from samples of SNe Ic-BL. Rest-frame wavelengths are shown on x-axis, and phases are on y-axis. The samples include SNe Ic-BL with associated GRBs (cross data points), and without GRB (dot data points). Phase is referred from the GRB trigger. The samples show the evolution of CaIR3 peaks from blue to red with ages, and the peaks are well constrained within the CaIR3 constraint if considering late-photospheric phases between 30 – 100 days; see Subsection 4 for more discussion. SN 2019oyw’s CaIR3 peaks are also shown in red (assuming $z = 0.0785$) and blue (assuming $z^* = 0.1051$). We noted that early data of SN 2019oyw from VLT/FORS (see Subsection 2.3). The plot shows that assuming $z^* = 0.1051$ improves the feature alignment better than $z = 0.0785$.

5. PHYSICAL SCENARIOS

The result of redshift $z^* = 0.1051$ showing best alignment challenges our understanding of this event. GRB 190829A/SN 2019oyw superposed on the galaxy SDSS J025810.28-085719.2, and that galaxy’s gas imposed absorption lines detected in the early afterglow (Hu et al. 2021). Therefore, assigning this galaxy as the host and adopting redshift $z = 0.0785$ was intuitive. However, if this was correct, the evidence presented here would imply that SN 2019oyw is a very unusual object.

If the SN 2019oyw is actually in a host at a redshift of $z = 0.0785$, the observed CaIR3 peak of SN 2019oyw corresponds to a peculiar velocity with respect to the galaxy of $\sim 4,000$ km/s in the radial direction away from the observer. Physically, this might be explained by an apparent asymmetry in the SN expansion such that line-emitting materials with high velocities away from us were dominating the observations. However, this implies that what we are seeing is dominated by light from the far side. Considering that the light from the far side should be more attenuated and obscured due to the intervening material on the closer side, how this scenario can explain the observation is uncertain.

Another possible explanation is that the explosion occurred in a progenitor with an exceptionally high proper velocity. In a 3-body interaction (Brown 2015), a binary (each with $3 M_{\odot}$, with semi-major axis of the binary 0.5 AU) interacting with a massive black hole ($\sim 10^6 M_{\odot}$) can disrupt one of the binary and eject the other with final

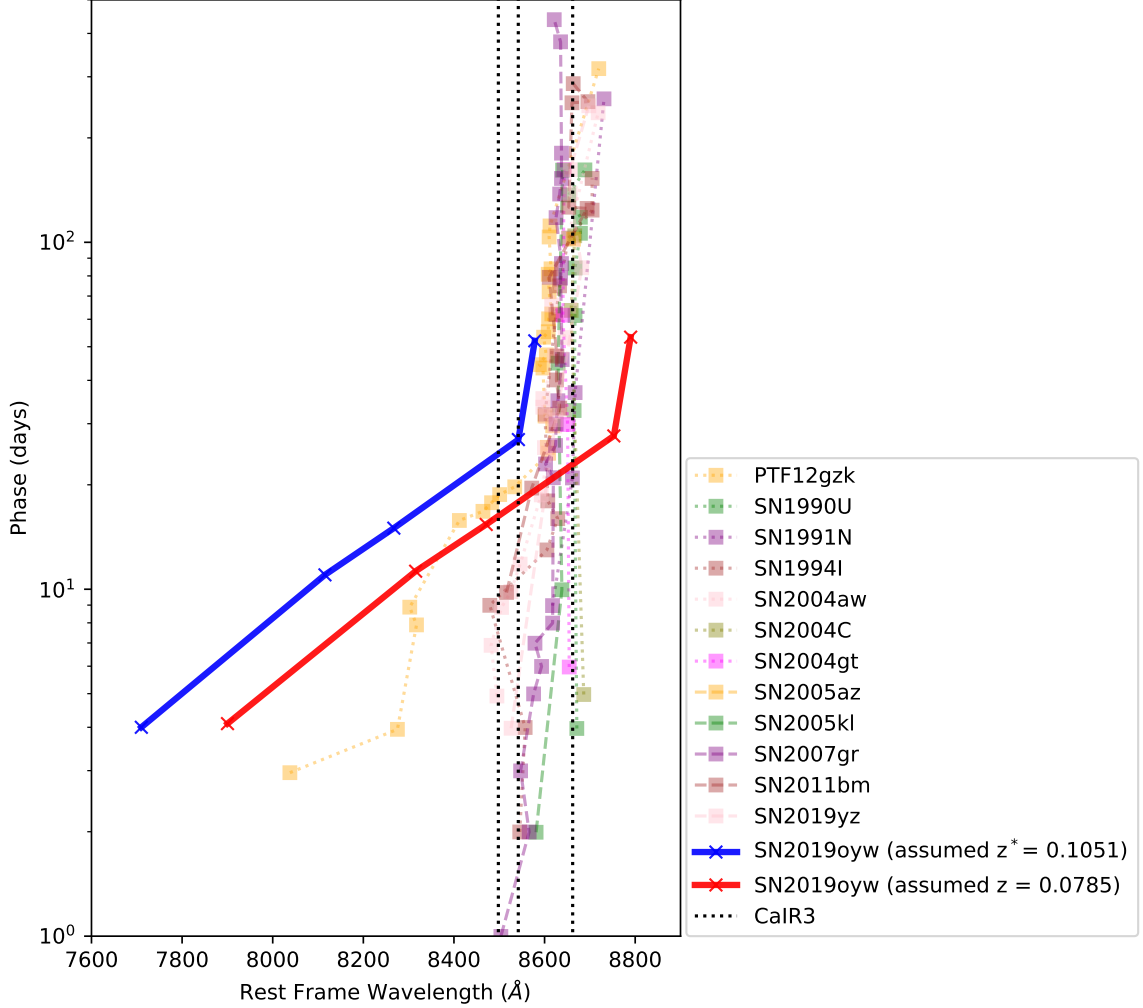


Figure 14. Similar to Figure 13 but with a sample of SNe Ic (square data points) instead. We note that phase is referred from the date of discovery for these SNe without associated GRB.

velocity at infinite distance of the order of 1,000 km/s. We note that the estimated ejected velocity increases with the mass of the black hole M and the mass of the binary system, m_b as $M^{1/6}m_b^{1/3}$. For this event, the progenitor of GRB 190829A was a massive star (i.e., $\gtrsim 20 M_\odot$ at zero-age main sequence; [Levan et al. \(2016\)](#)). The SDSS galaxy has nuclear emission line ratios ([Izzo et al. \(in prep.\)](#) and [Patricia Schady](#) via personal communication), which imply the presence of an AGN, which therefore implies a supermassive black hole likely more massive than $10^7 M_\odot$ ([Woo & Urry 2002](#)).

However, the progenitor need not have an exceptional proper motion with respect to its host galaxy, if in actuality it was in a dwarf galaxy situated behind the apparent SDSS galaxy. We note that recent studies show evidence such as very high stellar mass ([Gupta et al. 2022](#)) and the presence of AGN supporting that, if the SDSS galaxy is the host of the long GRB 190829A, it would be atypical one for a long GRB host ([Perley et al. 2016](#)).

In Figure 4 we show at the location of the burst the template images taken from *HST*/WFC3 during January 2021 (i.e., about 500 days after the burst in the observing frame). In these images, SN 2019oyw had faded below the detection levels of the telescope. The red circle in each image shows an aperture of 0.39 arcsecond in radius centered on the supernova, using the last detection as a reference. In the vicinity of the burst location, we observed a dust lane extending from north to south on the west. We note a bright clump at the western edge of the red circle in the F125W and F140W NIR images. However, the template images do not show a clear evidence of any dwarf galaxy behind the SDSS galaxy at the burst location.

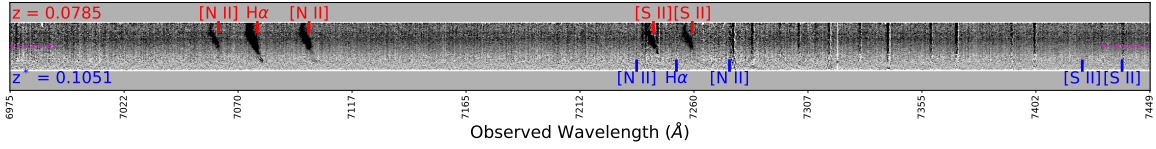


Figure 15. Two-dimensional spectrum at the location of GRB 190829A/SN 2019oyw taken by X-shooter. The location of the transient was placed at the center of the slit (horizontal magenta dotted lines). X-axis is shown in observed wavelengths. The spectrum is shown in the middle, and line markers are shown at the top for assuming $z = 0.0785$ (red) and bottom for $z^* = 0.1051$ (blue). These markers include $H\alpha$ λ 6563 Å, [N II] $\lambda\lambda$ 6548, 6583 Å, and [S II] $\lambda\lambda$ 6717, 6731 Å. The image is shown in inverse color, i.e., black = bright. The observed lines are consistent with the SDSS J025810.28-085719.2 at the redshift $z = 0.0785$. See more details about this observation in Izzo et al. (in prep.).

We show in Figure 15 the 2D spectrum taken from X-shooter Izzo et al. (in prep.). The spectrum shows emission lines including $H\alpha$, [N II], and [S II] corresponding to the SDSS galaxy at $z = 0.0785$. These are marked in red. Marked in blue are the expected locations of the same set of lines assuming $z^* = 0.1051$. We note that these lines are strong emission lines typically observed in star-forming galaxies (Kewley & Ellison 2008), which are the preferred hosts of GRB-SN events (Fruchter et al. 2006; Modjaz et al. 2020). As can be seen in Figure 15 the spectrum reveals no clear sign of a more distant galaxy.

The non-detection does not completely reject the possibility of an existing dwarf galaxy at $z^* = 0.1051$ because it could be hidden behind the bright and dusty foreground SDSS galaxy (Gupta et al. 2022). From the 2D spectrum, we can place an upper limit if there was a point source, such as a bright H II region, emitting $H\alpha$ from $z^* = 0.1051$. The estimated root mean square of the sky region around 7,253 Å (i.e., $H\alpha$ at z^*) is 3.37×10^{-19} erg/s/cm²/Å in a pixel. This is equivalent to the observing upper limit about 6.88×10^{-18} erg/s/cm² in the integrated flux assuming a point source.⁶

We note that in this scenario the $H\alpha$ emission from $z^* = 0.1051$ passes through the SDSS foreground galaxy at $z = 0.0785$ before being observed by the telescope. Since the attenuation of the $H\alpha$ emission is mostly due to the SDSS galaxy, the dilated wavelength of the $H\alpha$ emission arriving at the SDSS galaxy would be redshifted by about $z' \approx 0.0247$ (i.e., shifted to $\sim 6,725$ Å). By assuming $A_V = 2.33$ estimated from the afterglow (Zhang et al. 2021), the extinction factor is ~ 0.18 . This implies the extinction-corrected upper limit 3.82×10^{-17} erg/s/cm². This is equivalent to 1.08×10^{39} erg/s (luminosity distance to $z^* = 0.1051$ is 487 Mpc). By comparing this upper limit to the H II region luminosity function observed from nineteen nearby spiral galaxies (Santoro et al. 2022), this upper limit is at the percentile between 86th to 99th (with average 94th). This implies that about 90 percent of these regions would be undetected considering the current upper limit.

It is perhaps interesting to ask what we would see if GRB 190829A/SN 2019oyw had gone off on a host like that of GRB 980425/SN 1998bw. The *HST* has an angular resolution approximately ten times better than ground-based imaging. Therefore, *HST* imaging of the host of GRB 190829A/SN 2019oyw has roughly the same physical resolution as ground-based imaging of the host of GRB 980425/SN 1998bw, ESO 184-G82, at $z = 0.0085$, whose H II regions were studied by Christensen et al. (2008). If we assume the missing distant galaxy at $z^* = 0.1051$ to be similar to the SN 1998bw’s host, we can compare the estimated upper limit. The study found varied $H\alpha$ strengths of the H II regions spanning from about $\sim 10^{37}$ to 10^{39} erg/s. All but one of these roughly two-dozen H II regions would be $\lesssim 1\sigma$ sources in our observations were they in the hypothesized dwarf host of SN 2019oyw. Thus, to find no such source would not be too surprising.

Finally, we note that if SN 2019oyw occurred at $z^* \sim 0.1$ rather than $z = 0.785$ its r-band absolute magnitude would be about 0.5 magnitude brighter than SN 1998bw instead of matching it closely (Medler (2023)). However, some SNe Ic-BL both with (Schulze et al. 2014; Toy et al. 2016; Srinivasaragavan et al. 2024) and without (Taddia et al. 2019) a known GRB association have been this bright. Furthermore, Medler (2023) finds that when SN 2019oyw is assumed to be at the redshift of the large $z = 0.0785$ spiral, its pseudobolometric luminosity is somewhat less than that of SN 1998bw; however, we calculate that if instead it were at $z^* = 0.1051$ its pseudobolometric luminosity would agree with that of SN 1998bw to within a couple of percents. Thus, the luminosity of the SN does not cause us to strongly prefer one distance solution over the other.

⁶ For this observation from X-shooter (more details in Izzo et al. (in prep.)), the wavelength dispersion (x-axis) is 2 Å/pix with 5.7 pix/FWHM (full-width half maximum; Vernet et al. (2011)). We assumed a point-spread function of 0.7 arcsecond/FWHM (Schönebeck et al. 2014), which is equivalent to 4.375 pixels/FWHM given 0.16 arcsecond/pixel in the cross-dispersion direction (y-axis).

6. DISCUSSION AND SUMMARY

GRB 190829A/SN 2019oyw was observed between 2019-09-28 and 2021-01-09 using the *HST*/WFC3. Images and spectra of the transient showed a clear sign of the fading SN 2019oyw in both optical and NIR. Its late-time light curve faded with the decay rate consistent with Co^{56} powering mechanism (Figure 5), typical for late-time GRB-SNe (Woosley & Heger 2006) until the last detection on 2020-02-16. The spectra (Figure 8) showed broad P-Cygni profiles which narrowed and de-blended with time. In particular, two prominent peaks marked as ‘A’ and ‘B’ in figures were clearly visible. We attempted to identify the features by aligning the spectra against that of the standard GRB-SN 1998bw. However, we found that the spectral features were redshifted by about 4,000 km/s from the redshift of the large foreground SDSS spiral whose absorption features are observed in the afterglow spectra of GRB 190829A, $z = 0.0785$. This velocity offset can be best measured using the Ca II NIR triplet $\lambda\lambda$ 8498, 8542, 8662 Å (CaIR3) emission, but is also seen near the He I λ 10830 Å feature and the overall shape of the NIR spectrum (see Figure 9). This widespread shift makes the idea that we are seeing an unusual blending of lines appear unlikely.

To better understand the behavior of the spectra, we analyzed the CaIR3 evolution in a large sample of Type Ic-BL and Ic SNe from the literature (Figures 13 and 14, respectively). From the samples, we highlighted key observations (see Section 4). The samples show that a CaIR3 peak evolve from blue to red with time, with this evolution being particularly rapid at early photospheric phases when the peak is observed to be bluer than the bluest line in the triplet (i.e., 8,498 Å). Inside the interval (i.e., 8,498 – 8,662 Å), the peak evolves more slowly, as the curve turns nearly vertical. The CaIR3 peaks are well constrained within the interval during late photospheric phases starting at about 30 days. The comparison to the samples showed no other object with the CaIR3 line as red as that of SN 2019oyw were it truly at the redshift of the SDSS galaxy. Assuming instead that SN 2019oyw behaved similarly to the SNe in the samples, we re-estimated the redshift to be $0.0944 \leq z^* \leq 0.1156$. With this new alignment, we confidently identified the feature ‘A’ as the Ca II NIR triplet $\lambda\lambda$ 8498, 8542, 8662 Å. In contrast, we cannot be certain which spectral features are associated with the feature ‘B’. Without the detection of other He I lines such as He I 2.058 μm we cannot confirm the associate of the feature ‘B’ with He I rather than other features such as Mg II (Bufano et al. 2012; Chornock et al. 2010; Izzo et al. 2019; Lucy 1991; Mazzali & Lucy 1998; Patat et al. 2001; Taubenberger et al. 2006).

As GRB 190829A/SN 2019oyw is superposed on the galaxy SDSS J025810.28-085719.2 whose gas was seen in Ca II H/K absorption in the early afterglow, assigning this galaxy as the host was intuitive. However, our surprising result challenges this picture. If the SDSS galaxy is its actual host, the evidence implies that SN 2019oyw was very unusual. The redshifted features offset by 4,000 km/s could be a consequence from an observing asymmetry such that the line-emitting materials from the far side (i.e., moving away from observers) were dominating the observations. It is far from obvious about how one gets the dominance of the far side. Another possible explanation (see Section 5) involves a progenitor with high velocity such as one that would be produced by a 3-body interaction of a tight and massive binary and a supermassive black hole (Brown 2015). We note that the presence of an AGN was observed in the SDSS galaxy (Izzo et al. (in prep.) and Patricia Schady via personal communication), which implies the presence of a supermassive black hole likely more massive than $10^7 M_{\odot}$ (Woo & Urry 2002).

Instead, if we placed the explosion further behind the SDSS galaxy on a smaller dwarf galaxy at z^* , the observed discrepancies could be straightforwardly resolved. In this scenario, the spectral features of SN 2019oyw evolved similarly to other SNe Ic-BL and Ic in the comparison samples. Given that the SDSS galaxy is bright and dusty, especially at the location of the event, searching for a more distant dwarf host would be challenging. The available images from *HST* and the spectra from the X-shooter show no sign of such a system. We note that these observations were not designed to see beyond the foreground SDSS galaxy, and were done before we knew about this surprising evidence. We estimate the upper limit of the $\text{H}\alpha$ emission from a bright H II region in a background galaxy at z^* , and show that our non-detection does not by any means rule out the presence of such a host. We encourage further investigation with a design that can overcome observing challenges and see beyond the bright and dusty SDSS galaxy, such as a radio search for H I emission from the potential dwarf host.

In summary, we present a surprising result on the origins of the nearby GRB 190829A. Our story is similar to GRB 020819B (Perley et al. 2017) and GRB 130702A (Kelly et al. 2013) in that there is new evidence supporting a possible revision of the assigned host of the event. The possible need for such a revision is not a total surprise as several studies had already pointed out that the SDSS galaxy is quite atypical for a long-duration GRB host. In particular, the SDSS galaxy was estimated to have stellar mass on the order of $10^{12} M_{\odot}$ (Gupta et al. 2022), very massive for a long GRB host. There is also evidence indicating the presence of AGN from the galaxy, which is atypical

for a long GRB host. However, if the explosion was behind the foreground spiral, GRB 190829A/SN 2019oyw could be one among the typical cases like GRB 980425/SN 1998bw (Galama et al. 1998).

Finally, the work here provided insights into the time evolution of GRB-SNe and a potential method for directly determining the redshift of a GRB-SN. We demonstrated in Section 4 that using the CaIR3 feature has advantages due to the strong signal strength, stability and slow evolution during late photospheric phase from phase about 30 – 100 days. The accuracy of this method is of the order of 1,000 km/s. We encourage further studies of the use of CaIR3 for the redshift estimation. In contrast to other existing methods (Li et al. 2023), this method allows us to estimate the redshift of the explosion using the lines of the associated supernova. Furthermore, since CaIR3 is a common feature typically observed in a supernova regardless of its class (Marion et al. 2009; Cano et al. 2014; Gutiérrez et al. 2017; Modjaz et al. 2016; Prentice et al. 2022; Silverman et al. 2015; van Rossum 2012), the use of CaIR3 for redshift estimation could benefit not only the cases of GRB-SNs, but also potentially other calcium-rich transients.

This research is based on observations made with NASA/ESA Hubble Space Telescope obtained from the Space Telescope Science Institute, which is operated by the Association of Universities for Research in Astronomy, Inc., under NASA contract NAS 5–26555. The *HST* observations presented here were taken under General Observer(GO) Programs 15089, 15510, 16042, and 16320. Support for K. Bhirombhakdi was provided through grants associated with GO Programs 15510, 16042 and 16320 from the STScI under NASA contract NAS5-26555.

This research made use of Photutils, an Astropy package for detection and photometry of astronomical sources (Bradley et al. 2021).

This work made use of the data products generated by the Modjaz group (formerly NYU SN group), and released under DOI:10.5281/zenodo.58766 (Liu et al. 2016), available at <https://github.com/nyusngroup/SESNTemple/>.

KB thanks Dr. Robert Quimby for sharing his code that performs the generalized Savitzky-Golay method (Quimby et al. 2018).

S. B. acknowledge support from the PRIN-INAF 2022 project “Shedding light on the nature of gap transients: from the observations to the model”

This project was conducted during the pandemic of COVID-19. We would like to thank every individual both inside and outside the scientific communities, for all the efforts during this hard time. And, we would like to offer our deepest and most sincere condolences for every loss.

APPENDIX

A. USING CROSS CORRELATION TO DETERMINE REDSHIFT OF SN 2019OYW

In this section, we present our use of cross-correlation (Blondin & Tonry 2007) to estimate the redshift of SN 2019oyw. Our aim was to perform the cross correlation around the CaIR3 emission of SN 1998bw and the feature ‘A’ of SN 2019oyw as shown in Figures 9 and 10. The epoch 2019-10-26 was chosen for the computation to limit the complication from line blending, as the feature is relatively narrow and high SNR at this epoch. The epoch 1998-06-24 of SN 1998bw (Patat et al. 2001), which is at a comparable phase, was chosen as the GRB-SN template (Cano et al. 2014; Modjaz et al. 2016).

We implemented our code to perform the cross correlation following Blondin & Tonry (2007), except that we did a direct cross-correlation on the data, rather than transforming to Fourier space. Both source and template spectra were extinction corrected. Following Blondin & Tonry (2007) both spectra were smoothed prior to cross-correlation. We used the generalized Savitsky-Golay method (Quimby et al. (2018) using the same parameters as for our earlier spectral reduction (see Section 2.2 for the parameters). The template spectrum was normalized with respect to its CaIR3 peak, and the source to its feature ‘A’. Due to limitation on the template spectrum longer than 8,800 Å (rest-frame) and on the source shorter than 9,100 Å (observed frame), we chose to include data points surrounding the peak of the feature ‘A’ (approximately 9,300 to 9,700 Å in the observed frame, or 8,400 to 8,800 Å in the rest-frame assuming $z^* = 0.1051$ as shown in Figure 16 LEFT).

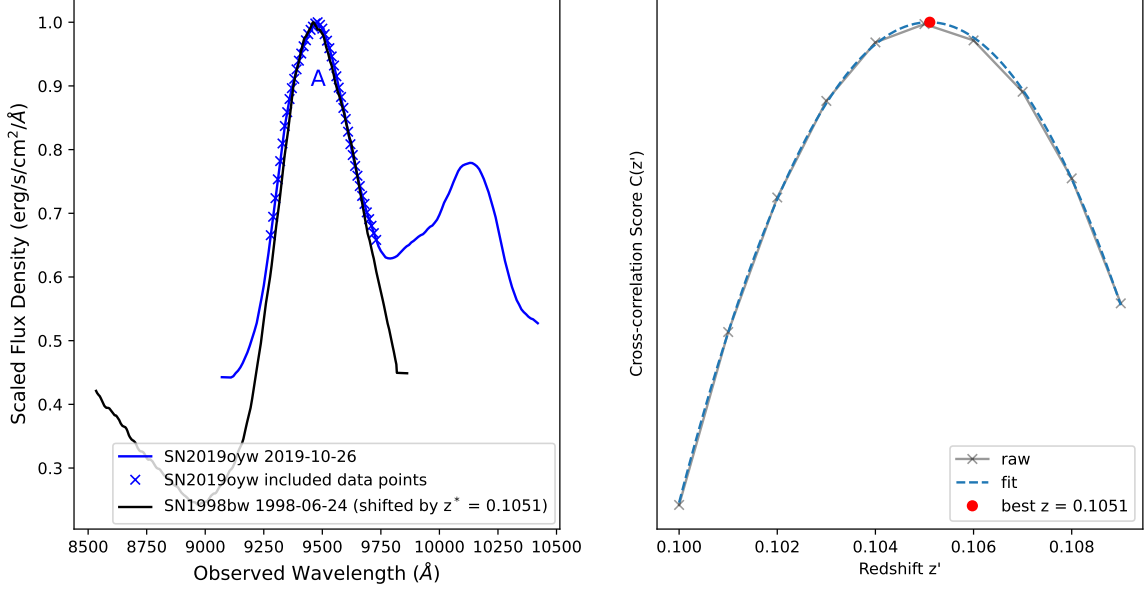


Figure 16. Cross correlation matching CaIR3 peaks. LEFT: The cross correlation technique was performed using SN 2019oyw on epoch 2019-10-26 (source, blue) and SN 1998bw on epoch 1998-06-24 (template, black). For the template, this peak was identified as CaIR3 (Patat et al. 2001). For the source, only included data points around the peak (blue crosses) were used in the computation. For more details, see Appendix A. RIGHT: The optimal solution z^* from the cross-correlation (red dot) is estimated by the second-order polynomial fit to the cross-correlation score curve.

We performed the cross correlation by assuming the redshift $z' \in [0.100, 0.109]$ with a step of 0.001. The cross-correlation score $C(z = z')$ showed a strictly concave profile, which was fit by a second-order polynomial to locate the optimal solution. As shown in Figure 16, the optimal solution is $z^* = 0.1051 \pm 0.0009$ as shown in Figure 16 RIGHT.

REFERENCES

- Abdalla, H., Adam, R., Aharonian, F., et al. 2019, *Nature*, 575, 464, doi: [10.1038/s41586-019-1743-9](https://doi.org/10.1038/s41586-019-1743-9)
- Abdurro'uf, Accetta, K., Aerts, C., et al. 2022, *ApJS*, 259, 35, doi: [10.3847/1538-4365/ac4414](https://doi.org/10.3847/1538-4365/ac4414)
- Amati, L. 2006, *MNRAS*, 372, 233, doi: [10.1111/j.1365-2966.2006.10840.x](https://doi.org/10.1111/j.1365-2966.2006.10840.x)
- ANTARES Collaboration, Albert, A., André, M., et al. 2021, *JCAP*, 2021, 092, doi: [10.1088/1475-7516/2021/03/092](https://doi.org/10.1088/1475-7516/2021/03/092)
- Appenzeller, I., Fricke, K., Fürtig, W., et al. 1998, *The Messenger*, 94, 1
- Astropy Collaboration, Robitaille, T. P., Tollerud, E. J., et al. 2013, *A&A*, 558, A33, doi: [10.1051/0004-6361/201322068](https://doi.org/10.1051/0004-6361/201322068)
- Astropy Collaboration, Price-Whelan, A. M., Sipőcz, B. M., et al. 2018, *AJ*, 156, 123, doi: [10.3847/1538-3881/aabc4f](https://doi.org/10.3847/1538-3881/aabc4f)
- Ben-Ami, S., Gal-Yam, A., Filippenko, A. V., et al. 2012, *ApJL*, 760, L33, doi: [10.1088/2041-8205/760/2/L33](https://doi.org/10.1088/2041-8205/760/2/L33)
- Blanch, O., Longo, F., Berti, A., et al. 2020, *GRB Coordinates Network*, 29075, 1
- Blondin, S., & Tonry, J. L. 2007, *ApJ*, 666, 1024, doi: [10.1086/520494](https://doi.org/10.1086/520494)
- Bradley, L., Sipőcz, B., Robitaille, T., et al. 2020, *astropy/photutils: 1.0.0*, 1.0.0, Zenodo, doi: [10.5281/zenodo.4044744](https://doi.org/10.5281/zenodo.4044744)
- Brown, W. R. 2015, *ARA&A*, 53, 15, doi: [10.1146/annurev-astro-082214-122230](https://doi.org/10.1146/annurev-astro-082214-122230)
- Bufano, F., Pian, E., Sollerman, J., et al. 2012, *ApJ*, 753, 67, doi: [10.1088/0004-637X/753/1/67](https://doi.org/10.1088/0004-637X/753/1/67)
- Cano, Z., de Ugarte Postigo, A., Pozanenko, A., et al. 2014, *A&A*, 568, A19, doi: [10.1051/0004-6361/201423920](https://doi.org/10.1051/0004-6361/201423920)
- Chand, V., Banerjee, A., Gupta, R., et al. 2020, *ApJ*, 898, 42, doi: [10.3847/1538-4357/ab9606](https://doi.org/10.3847/1538-4357/ab9606)
- Chornock, R., Berger, E., Levesque, E. M., et al. 2010, *arXiv e-prints*, arXiv:1004.2262. <https://arxiv.org/abs/1004.2262>
- Christensen, L., Vreeswijk, P. M., Sollerman, J., et al. 2008, *A&A*, 490, 45, doi: [10.1051/0004-6361:200809896](https://doi.org/10.1051/0004-6361:200809896)
- de Naurois, M. 2019, *The Astronomer's Telegram*, 13052, 1
- de Ugarte Postigo, A., Izzo, L., Thoene, C. C., et al. 2019, *GRB Coordinates Network*, 25677, 1

- Dichiara, S., Bernardini, M. G., Burrows, D. N., et al. 2019, GRB Coordinates Network, 25552, 1
- Dichiara, S., Troja, E., Lipunov, V., et al. 2022, MNRAS, 512, 2337, doi: [10.1093/mnras/stac454](https://doi.org/10.1093/mnras/stac454)
- Dressel, L. 2021, Wide Field Camera 3 Instrument Handbook, Version 13.0
- Duan, M.-Y., & Wang, X.-G. 2019, ApJ, 884, 61, doi: [10.3847/1538-4357/ab3c6e](https://doi.org/10.3847/1538-4357/ab3c6e)
- Fermi GBM Team. 2019, GRB Coordinates Network, 25551, 1
- Fraija, N., Veres, P., Beniamini, P., et al. 2021, ApJ, 918, 12, doi: [10.3847/1538-4357/ac0aed](https://doi.org/10.3847/1538-4357/ac0aed)
- Fruchter, A. S., & Hook, R. N. 2002, PASP, 114, 144, doi: [10.1086/338393](https://doi.org/10.1086/338393)
- Fruchter, A. S., Levan, A. J., Strolger, L., et al. 2006, Nature, 441, 463, doi: [10.1038/nature04787](https://doi.org/10.1038/nature04787)
- Galama, T. J., Vreeswijk, P. M., van Paradijs, J., et al. 1998, Nature, 395, 670, doi: [10.1038/27150](https://doi.org/10.1038/27150)
- Gupta, R., Pandey, S. B., Kumar, A., et al. 2022, Journal of Astrophysics and Astronomy, 43, 82, doi: [10.1007/s12036-022-09865-0](https://doi.org/10.1007/s12036-022-09865-0)
- Gutiérrez, C. P., Anderson, J. P., Hamuy, M., et al. 2017, ApJ, 850, 89, doi: [10.3847/1538-4357/aa8f52](https://doi.org/10.3847/1538-4357/aa8f52)
- H. E. S. S. Collaboration, Abdalla, H., Aharonian, F., et al. 2021, Science, 372, 1081, doi: [10.1126/science.abe8560](https://doi.org/10.1126/science.abe8560)
- Hu, Y. D., Castro-Tirado, A. J., Kumar, A., et al. 2021, A&A, 646, A50, doi: [10.1051/0004-6361/202039349](https://doi.org/10.1051/0004-6361/202039349)
- Izzo, L., de Ugarte Postigo, A., Maeda, K., et al. 2019, Nature, 565, 324, doi: [10.1038/s41586-018-0826-3](https://doi.org/10.1038/s41586-018-0826-3)
- Japelj, J., Vergani, S. D., Salvaterra, R., et al. 2018, A&A, 617, A105, doi: [10.1051/0004-6361/201833209](https://doi.org/10.1051/0004-6361/201833209)
- Kelly, P. L., Filippenko, A. V., Fox, O. D., Zheng, W., & Clubb, K. I. 2013, ApJL, 775, L5, doi: [10.1088/2041-8205/775/1/L5](https://doi.org/10.1088/2041-8205/775/1/L5)
- Kelly, P. L., Filippenko, A. V., Modjaz, M., & Kocevski, D. 2014, ApJ, 789, 23, doi: [10.1088/0004-637X/789/1/23](https://doi.org/10.1088/0004-637X/789/1/23)
- Kewley, L. J., & Ellison, S. L. 2008, ApJ, 681, 1183, doi: [10.1086/587500](https://doi.org/10.1086/587500)
- Kuemmel, M. W., Walsh, J. R., Larsen, S. S., & Hook, R. N. 2005, in Astronomical Society of the Pacific Conference Series, Vol. 347, Astronomical Data Analysis Software and Systems XIV, ed. P. Shopbell, M. Britton, & R. Ebert, 138
- Kuntschner, H., Kümmel, M., Walsh, J. R., & Bushouse, H. 2011, Revised Flux Calibration of the WFC3 G102 and G141 grisms, Space Telescope WFC Instrument Science Report
- Levan, A., Crowther, P., de Grijs, R., et al. 2016, SSRv, 202, 33, doi: [10.1007/s11214-016-0312-x](https://doi.org/10.1007/s11214-016-0312-x)
- Li, L., Wang, Y., Shao, L., et al. 2018, ApJS, 234, 26, doi: [10.3847/1538-4365/aaa02a](https://doi.org/10.3847/1538-4365/aaa02a)
- Li, M., Kang, Z., Wu, C., et al. 2023, Frontiers in Astronomy and Space Sciences, 10, 1124317, doi: [10.3389/fspas.2023.1124317](https://doi.org/10.3389/fspas.2023.1124317)
- Lipunov, V., Balakin, F., Gorbovskoy, E., et al. 2019, GRB Coordinates Network, 25652, 1
- Liu, Y.-Q., Bianco, F. B., & Modjaz, M. 2016, SESNtemple: First Public Release, Zenodo, doi: [10.5281/ZENODO.58766](https://doi.org/10.5281/ZENODO.58766)
- Lucy, L. B. 1991, ApJ, 383, 308, doi: [10.1086/170787](https://doi.org/10.1086/170787)
- MAGIC Collaboration, Acciari, V. A., Ansoldi, S., et al. 2019, Nature, 575, 455, doi: [10.1038/s41586-019-1750-x](https://doi.org/10.1038/s41586-019-1750-x)
- Marion, G. H., Höflich, P., Gerardy, C. L., et al. 2009, AJ, 138, 727, doi: [10.1088/0004-6256/138/3/727](https://doi.org/10.1088/0004-6256/138/3/727)
- Mazzali, P. A., & Lucy, L. B. 1998, MNRAS, 295, 428, doi: [10.1046/j.1365-8711.1998.01323.x](https://doi.org/10.1046/j.1365-8711.1998.01323.x)
- Medler, K. 2023, PhD thesis, Liverpool John Moores University. <http://researchonline.ljmu.ac.uk/id/eprint/21959/>
- Modjaz, M., Liu, Y. Q., Bianco, F. B., & Graur, O. 2016, ApJ, 832, 108, doi: [10.3847/0004-637X/832/2/108](https://doi.org/10.3847/0004-637X/832/2/108)
- Modjaz, M., Bianco, F. B., Siwek, M., et al. 2020, ApJ, 892, 153, doi: [10.3847/1538-4357/ab4185](https://doi.org/10.3847/1538-4357/ab4185)
- Nakamura, T., Mazzali, P. A., Nomoto, K., & Iwamoto, K. 2001, ApJ, 550, 991, doi: [10.1086/319784](https://doi.org/10.1086/319784)
- Oates, S. R., Dichiara, S., & Swift/UVOT Team. 2019, GRB Coordinates Network, 25570, 1
- Patat, F., Cappellaro, E., Danziger, J., et al. 2001, ApJ, 555, 900, doi: [10.1086/321526](https://doi.org/10.1086/321526)
- Perley, D. A., Niino, Y., Tanvir, N. R., Vergani, S. D., & Fynbo, J. P. U. 2016, SSRv, 202, 111, doi: [10.1007/s11214-016-0237-4](https://doi.org/10.1007/s11214-016-0237-4)
- Perley, D. A., Krühler, T., Schady, P., et al. 2017, MNRAS, 465, L89, doi: [10.1093/mnras/rlw221](https://doi.org/10.1093/mnras/rlw221)
- Prentice, S. J., Maguire, K., Siebenaler, L., & Jerkstrand, A. 2022, MNRAS, 514, 5686, doi: [10.1093/mnras/stac1657](https://doi.org/10.1093/mnras/stac1657)
- Quimby, R. M., De Cia, A., Gal-Yam, A., et al. 2018, ApJ, 855, 2, doi: [10.3847/1538-4357/aaac2f](https://doi.org/10.3847/1538-4357/aaac2f)
- Ravasio, M. E., Oganessian, G., Salafia, O. S., et al. 2019, A&A, 626, A12, doi: [10.1051/0004-6361/201935214](https://doi.org/10.1051/0004-6361/201935214)
- Sahu, K. C., & et al. 2021, WFC3 Data Handbook v. 5.0
- Salafia, O. S., Ravasio, M. E., Yang, J., et al. 2022, ApJL, 931, L19, doi: [10.3847/2041-8213/ac6c28](https://doi.org/10.3847/2041-8213/ac6c28)
- Santoro, F., Kreckel, K., Belfiore, F., et al. 2022, A&A, 658, A188, doi: [10.1051/0004-6361/202141907](https://doi.org/10.1051/0004-6361/202141907)
- Sato, Y., Obayashi, K., Theodore Zhang, B., et al. 2023, Journal of High Energy Astrophysics, 37, 51, doi: [10.1016/j.jheap.2022.12.004](https://doi.org/10.1016/j.jheap.2022.12.004)

- Schlaflly, E. F., & Finkbeiner, D. P. 2011, *ApJ*, 737, 103, doi: [10.1088/0004-637X/737/2/103](https://doi.org/10.1088/0004-637X/737/2/103)
- Schönebeck, F., Puzia, T. H., Pasquali, A., et al. 2014, *A&A*, 572, A13, doi: [10.1051/0004-6361/201424196](https://doi.org/10.1051/0004-6361/201424196)
- Schulze, S., Malesani, D., Cucchiara, A., et al. 2014, *A&A*, 566, A102, doi: [10.1051/0004-6361/201423387](https://doi.org/10.1051/0004-6361/201423387)
- Silverman, J. M., Vinkó, J., Marion, G. H., et al. 2015, *MNRAS*, 451, 1973, doi: [10.1093/mnras/stv1011](https://doi.org/10.1093/mnras/stv1011)
- Sim, S. A. 2017, in *Handbook of Supernovae*, ed. A. W. Alsabti & P. Murdin, 769, doi: [10.1007/978-3-319-21846-5_28](https://doi.org/10.1007/978-3-319-21846-5_28)
- Skrutskie, M. F., Cutri, R. M., Stiening, R., et al. 2006, *AJ*, 131, 1163, doi: [10.1086/498708](https://doi.org/10.1086/498708)
- Srinivasaragavan, G. P., Swain, V., O'Connor, B., et al. 2024, *ApJL*, 960, L18, doi: [10.3847/2041-8213/ad16e7](https://doi.org/10.3847/2041-8213/ad16e7)
- Taddia, F., Sollerman, J., Fremling, C., et al. 2019, *A&A*, 621, A71, doi: [10.1051/0004-6361/201834429](https://doi.org/10.1051/0004-6361/201834429)
- Taubenberger, S., Pastorello, A., Mazzali, P. A., et al. 2006, *MNRAS*, 371, 1459, doi: [10.1111/j.1365-2966.2006.10776.x](https://doi.org/10.1111/j.1365-2966.2006.10776.x)
- Toy, V. L., Cenko, S. B., Silverman, J. M., et al. 2016, *ApJ*, 818, 79, doi: [10.3847/0004-637X/818/1/79](https://doi.org/10.3847/0004-637X/818/1/79)
- Valeev, A. F., Castro-Tirado, A. J., Hu, Y. D., et al. 2019, *GRB Coordinates Network*, 25565, 1
- van Rossum, D. R. 2012, arXiv e-prints, arXiv:1208.3781. <https://arxiv.org/abs/1208.3781>
- Vernet, J., Dekker, H., D'Odorico, S., et al. 2011, *A&A*, 536, A105, doi: [10.1051/0004-6361/201117752](https://doi.org/10.1051/0004-6361/201117752)
- Volnova, A., Rumyantsev, V., Pozanenko, A., et al. 2019, *GRB Coordinates Network*, 25682, 1
- Woo, J.-H., & Urry, C. M. 2002, *ApJ*, 579, 530, doi: [10.1086/342878](https://doi.org/10.1086/342878)
- Woosley, S. E., & Bloom, J. S. 2006, *ARA&A*, 44, 507, doi: [10.1146/annurev.astro.43.072103.150558](https://doi.org/10.1146/annurev.astro.43.072103.150558)
- Woosley, S. E., & Heger, A. 2006, *ApJ*, 637, 914, doi: [10.1086/498500](https://doi.org/10.1086/498500)
- Yaron, O., & Gal-Yam, A. 2012, *PASP*, 124, 668, doi: [10.1086/666656](https://doi.org/10.1086/666656)
- Zhang, L.-L., Ren, J., Huang, X.-L., et al. 2021, *ApJ*, 917, 95, doi: [10.3847/1538-4357/ac0c7f](https://doi.org/10.3847/1538-4357/ac0c7f)